IRS-Assisted Aggregated VLC-RF System: Resource Allocation for Energy Efficiency Maximization

Nan An, Fang Yang, *Senior Member, IEEE*, Ling Cheng, *Senior Member, IEEE*, Jian Song, *Fellow, IEEE*, and Zhu Han, *Fellow, IEEE*

***Abstract*— Intelligent reflecting surface (IRS) alters the wireless channel by dynamically adjusting the propagation of wireless signals, thereby having the ability to enhance communication performance. Due to its low power consumption, IRS is expected to play an important role in improving energy efficiency (EE). In this paper, both optical IRS (OIRS) and radio frequency (RF) IRS are employed to assist aggregated visible light communication (VLC)-RF systems, and then a resource allocation algorithm is proposed to improve EE. To this end, a model for the IRS-assisted aggregated VLC-RF system is first established, followed by the formulated EE maximization problem. Furthermore, the EE maximization problem is decomposed into four subproblems, focusing on RF IRS configuration, optical subchannel assignment, OIRS arrangement, and joint power allocation. By employing block coordinate descent (BCD), the four subproblems are solved iteratively. Moreover, simulation results show the significant EE improvement brought by the IRS for aggregated VLC-RF systems. In addition, the convergence and effectiveness of the proposed BCD-based resource allocation algorithm, as well as the influence of key system parameters on EE are also demonstrated.**

***Index Terms*— Intelligent reflecting surface, OIRS, aggregated VLC-RF system, energy efficiency, block coordinate descent.**

Manuscript received 30 October 2023; revised 23 February 2024; accepted 18 April 2024. Date of publication 8 May 2024; date of current version 11 October 2024. This work was supported in part by Guangxi Science and Technology Major Program under Grant GUIKE AA23073006-1; in part by the National Science Foundation under Grant CNS-2107216, Grant CNS-2128368, Grant CMMI-2222810, and Grant ECCS-2302469; in part by JST ASPIRE under Grant JPMJAP2326; and in part by the U.S. Department of Transportation, Toyota and Amazon. An earlier version of this paper was presented in part at the IEEE ICC, 2024 [1]. The associate editor coordinating the review of this article and approving it for publication was A. Schmeink. *(Corresponding author: Fang Yang.)*

Nan An and Fang Yang are with the Department of Electronic Engineering, Beijing National Research Center for Information Science and Technology, Tsinghua University, Beijing 100084, China, and also with the Key Laboratory of Digital TV System of Guangdong Province and Shenzhen City, Research Institute of Tsinghua University in Shenzhen, Shenzhen 518057, China (e-mail: an21@mails.tsinghua.edu.cn; fangyang@tsinghua.edu.cn).

Ling Cheng is with the School of Electrical and Information Engineering, University of the Witwatersrand, Johannesburg 2050, South Africa (e-mail: ling.cheng@wits.ac.za).

Jian Song is with the Department of Electronic Engineering, Beijing National Research Center for Information Science and Technology, Tsinghua University, Beijing 100084, China, and also with Shenzhen International Graduate School, Tsinghua University, Shenzhen 518055, China (e-mail: jsong@tsinghua.edu.cn).

Zhu Han is with the Department of Electrical and Computer Engineering, University of Houston, Houston, TX 77004 USA, and also with the Department of Computer Science and Engineering, Kyung Hee University, Seoul 446701, South Korea (e-mail: hanzhu22@gmail.com).

Color versions of one or more figures in this article are available at https://doi.org/10.1109/TWC.2024.3393621.

Digital Object Identifier 10.1109/TWC.2024.3393621

I. Introduction

The rapid evolution of wireless communications has led to a substantial surge in the proliferation of devices connecting to wireless networks, which has led to a significant upswing in energy consumption [2]. Efforts to save energy have spurred interest in energy-efficient communication solutions, with visible light communication (VLC) emerging as a promising option [3]. Utilizing the unregulated visible light spectrum, information is transmitted while illumination is provided, where the energy consumed by communication also serves illumination, resulting in energy savings. Additionally, VLC leverages light-emitting diodes (LEDs), which are widely deployed in lighting infrastructure, as transmitters for information transmission. The receiving end employs photodiodes (PDs) to capture optical signals and demodulate information. As LEDs are inherently energy-efficient devices, VLC surpasses traditional radio frequency (RF) communication technologies in energy efficiency (EE) [4]. However, VLC relies on line-of-sight (LoS) communication links, resulting in limited coverage and susceptibility to signal blockage. Besides, users at the edge of VLC cells suffer from inter-cell interference from neighboring cells, leading to a decrease in achievable data rates.

In this case, VLC-RF coexisting systems have emerged as strong candidates for future wireless communications due to the complementary benefits of VLC and RF [5]. Specifically, VLC leverages the spectrum resources within the visible light band to alleviate the spectrum congestion of RF communications and improve EE, while RF can provide expansive coverage and alleviate inter-cell interference of VLC [6]. Additionally, VLC-RF coexisting systems can be categorized into hybrid VLC-RF systems and aggregated VLC-RF systems [7], [8]. In the former, each user is exclusively served by either a VLC access point (AP) or an RF AP, whereas in the latter, each user can be simultaneously served by both. Moreover, the aggregated VLC-RF system offers superior achievable data rates and more reliable communication compared to the hybrid VLC-RF system [7], [9]. To enhance the performance of the aggregated VLC-RF system, various resource allocation strategies should be developed, tailored to particular applications and services, while considering the distinct characteristics of VLC and RF systems. The primary communication metrics of paramount concern in the aggregated VLC-RF system encompass the achievable data rate [7], [10], [11] and EE [8], [12], [13], [14]. To improve the aforementioned communication metrics, a meticulous allocation of system resources, including power, bandwidth, and time slots, is typically necessary.

Recently, intelligent reflecting surface (IRS) has emerged as a novel paradigm in wireless communications, garnering significant research interest [6], [15]. IRS enables the reconfiguration of wireless channels by manipulating signal propagation, thereby offering a novel avenue for enhancing the transmission capability of wireless communications. Hence, extensive research has been conducted on optimizing various performance metrics in IRS-assisted systems, focusing on the joint optimization of resource allocation and IRS phases. To maximize the spectral efficiency (SE), the transmit powers and the IRS phases were jointly optimized in [16]. In [17] and [18], the IRS configuration methods were proposed to maximize the sum rate of the IRS-assisted multiple-input single-output and multiple-input multiple-output systems, respectively. In [19] and [20], IRS was employed to improve the signal-to-interference-plus-noise ratio (SINR) by jointly optimizing IRS phases and beamforming matrices. Additionally, considering the importance of physical layer security, the secrecy rate was maximized in [21] and [22] with carefully designed beamforming matrices and IRS phases. Moreover, the utilization of IRS has been observed in simultaneous wireless information and power transfer [23], mobile edge computing [24], and various other applications, indicating its significant potential.

Benefiting from the low energy consumption and cost-effectiveness characteristics of IRS units, IRS is anticipated to exert a substantial influence in enhancing the EE of communication systems. In RF systems, the challenge of EE maximization has been studied through the optimization of phase shifts, beamforming matrix, and transmit covariance matrix [25], [26], [27], and the intricate tradeoff between EE and SE has been revealed in [28]. In the context of VLC, optical IRS (OIRS) can create supplementary communication links by arranging its units, thereby alleviating the signal blockage problem [29] and enhancing SE of VLC systems with low energy consumption [30], [31]. In [32], the EE maximization problem of the OIRS-assisted VLC system was studied, confirming the potential of OIRS in improving EE.

To further improve EE, the OIRS and RF IRS are adopted into the aggregated VLC-RF system, which brings additional dimensions of resource, thereby significantly increasing the complexity of resource allocation. For the purpose of improving EE through comprehensively utilizing various resources, the design of resource allocation algorithms tailored for IRS-assisted aggregated systems is imperative. To address this issue, the system model is formulated first, and then the resource allocation algorithm is designed to improve EE. Specifically, the main contributions of this paper are summarized as follows.

- To the best of our knowledge, it is the first time to employ both OIRS and RF IRS to assist the aggregated VLC-RF system, and a comprehensive system model is established. Moreover, the EE maximization problem is formulated in detail with the consideration of various constraints present in the aggregated system.
- A block coordinate descent (BCD)-based resource allocation algorithm is proposed to improve EE. The overall problem is decomposed into four subproblems by BCD, focusing on RF IRS configuration, optical subchannel assignment, OIRS arrangement, and joint power allocation. Then, these subproblems are iteratively addressed by the gradient descent (GD) approach, Lagrangian relaxation heuristics (LRH) method, minorization-maximization (MM) algorithm, and Dinkelbach-based sequential fractional programming (SFP), respectively.
- The convergence and effectiveness of the proposed BCD-based resource allocation algorithm for the EE maximization problem are verified by comprehensive numerical simulations. Besides, compared to baselines, IRSs bring significant EE enhancement to the aggregated VLC-RF system. Moreover, the influence of key parameters on EE of the IRS-assisted aggregated system is also revealed.

The remainder of this paper is organized as follows. In Section II, the channel gain of the IRS-assisted aggregated VLC-RF system is described. Afterwards, the EE maximization problem is formulated in Section III, and the BCD-based resource allocation algorithm is proposed in Section IV. Numerical results are presented in Section V, and finally Section VI concludes this paper.

Notation: In this paper, scalars are denoted by normal letters (e.g., a and A), while vectors and matrices are represented as small and large boldface letters (e.g., $\boldsymbol{a}$ and $\boldsymbol{A}$), respectively. Besides, sets are expressed by fancy capital letters (e.g. $\mathcal{A}$). The element at the m-th row and the n-th column of the matrix $\boldsymbol{A}$ is represented as a_{mn}. All-zero matrix, m-dimensional all-zero vector, m-dimensional all-one vector, and the imaginary unit are denoted as $\boldsymbol{O}$, $\mathbf{0}_m$ $\mathbf{1}_m$, and j, respectively. Moreover, $(\cdot)^T$, $(\cdot)^H$, $(\cdot)^{-1}$, $(\cdot)^{\dagger}$, rank$(\cdot)$, and vec$(\cdot)$ are the symbols of transpose, Hermite transpose, inverse, Moore-Penrose pseudoinverse, rank, and vectorization operator of a matrix, respectively. In addition, $\|\cdot\|_F$, $\|\cdot\|_2$, $|\cdot|$, d, ∂, and $\lfloor\cdot\rfloor$ denote the symbols of Frobenius norm, 2-norm, absolute value, differential operator, partial operator, and floor operator, respectively. Besides, $\mathrm{diag}(\boldsymbol{a}_1, \ldots, \boldsymbol{a}_n)$ is a diagonal matrix with the k-th diagonal element of $\boldsymbol{a}_k, k \in \{1, 2, \ldots, n\}$. The fields of real number, complex number, and binary number are denoted by $\mathbb{R}$, $\mathbb{C}$, and $\mathbb{B}$, respectively. $\arg\min(\cdot)$ and $\arg\max(\cdot)$ are the arguments that make the following expression reach its minimum and maximum value, respectively.

II. System Model

The system model of the aggregated VLC-RF system is illustrated in Fig. 1, with a focus on the downlink vehicular communications. Multiple vehicles are randomly distributed

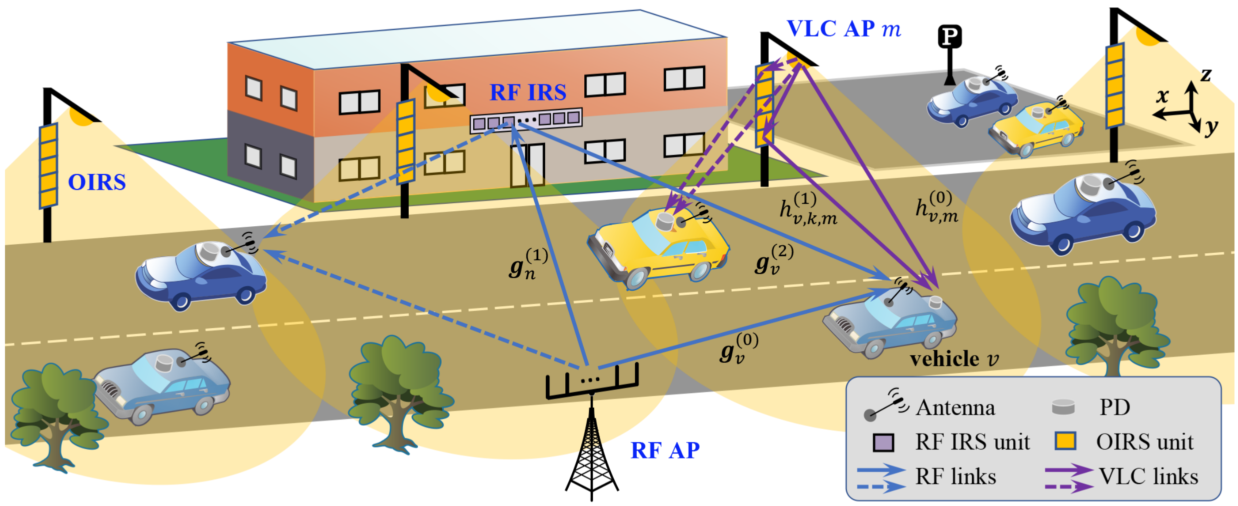

Fig. 1. System model of the proposed IRS-assisted aggregated VLC-RF system.

along a two-lane road, represented as $\mathcal{V} = \{1, 2, \ldots, V\}$. Besides, each vehicle is equipped with a PD and an antenna, enabling simultaneous service by both an RF AP and a VLC AP. Specifically, streetlamps serve as VLC APs, each equipped with an LED array and a K-unit OIRS on its lamppost. Owing to the consistency between uniform linear array (ULA) and lampposts in shape, OIRS units are arranged in the ULA form for deployment. Meanwhile, the RF AP is equipped with Z antennas arranged in a ULA, assisted by an N-unit RF IRS in the form of ULA. All units of an OIRS and the RF IRS are represented as $\mathcal{K} = \{1, 2, \ldots, K\}$ and $\mathcal{N} = \{1, 2, \ldots, N\}$, respectively. Besides, both VLC APs and the RF AP are attached to the centralized control unit, where the coordination and synchronization of RF and VLC are accomplished. In addition, based on the channel estimation method for the mobile scenario in [33], [34], and [35], it is assumed that the channel state information is known at the centralized control unit, and all configurations are decided uniformly and then executed at each AP.

A. VLC System

The set of VLC APs is denoted as $\mathcal{M} = \{1, 2, \ldots, M\}$, and the vehicles served by VLC AP m are renumerated and compose a set $\mathcal{V}_m = \{1, 2, \ldots, V_m\}$. To illustrate the association between VLC APs and vehicles, an association matrix $\boldsymbol{A} \in \mathbb{B}^{V\times M}$ is formulated, in which $a_{v,m} = 1$ and 0 indicate whether vehicle v is served by VLC AP m or not, respectively. Since streetlamps are arranged along the road and the illumination region of each streetlamp is limited, each vehicle is assumed to be served by its nearest VLC AP. For vehicle v, the serving VLC AP is $m_v = \arg\min_m u_{v,m}$, and thus the element of $\boldsymbol{A}$ is given by

$$a_{v,m} = \begin{cases} 1, & m = m_v, \\ 0, & \text{otherwise}. \end{cases} \tag{1}$$

VLC mainly relies on the LoS channel, while the non-line-of-sight (NLoS) channel can be neglected due to the weakness of diffuse reflection. The VLC channel gain from VLC AP m to vehicle v is characterized by the Lambertian model, which is expressed as

$$h^{(0)}_{v,m} = \begin{cases} \dfrac{(\kappa+1)\,\sigma_v \chi^2 \Upsilon}{2\pi u^2_{v,m} \sin^2(\psi_0)} \cos^{\kappa}(\varphi_{v,m}) \cos(\psi_{v,m}), \\ \qquad\qquad \text{if } 0 \le \psi_{v,m} \le \psi_0, \\ 0, \qquad\qquad \text{otherwise}, \end{cases} \tag{2}$$

where $u_{v,m}$, $\varphi_{v,m}$, and $\psi_{v,m}$ denote the distance between vehicle v and VLC AP m, the irradiance angle of the LED array on VLC AP m, and the incidence angle of the PD on vehicle v, respectively. Besides, κ, χ, σ_v, Υ, and ψ_0 represent the Lambertian index, the refractive index, the area of PD on vehicle v, the optical filter gain, and the semi-angle of PD's field-of-view, respectively.

With the help of OIRS, the OIRS-reflected channel is established. Based on the point source assumption [36], [37], the channel gain from VLC AP m to vehicle v reflected by the unit k of the m-th OIRS is expressed as

$$h^{(1)}_{v,k,m} = \begin{cases} \dfrac{F(\kappa+1)\sigma_v \chi^2 \Upsilon}{2\pi(u^{(1)}_{k,m} + u^{(2)}_{v,k})^2 \sin^2(\psi_0)} \cos^{\kappa}(\hat{\varphi}_{k,m}) \cos(\hat{\psi}_{v,k}), \\ \qquad\qquad \text{if } 0 \le \hat{\psi}_{v,k} \le \psi_0, \\ 0, \qquad\qquad \text{otherwise}, \end{cases} \tag{3}$$

where $u^{(1)}_{k,m}$, $u^{(2)}_{v,k}$, $\hat{\varphi}_{k,m}$, and $\hat{\psi}_{v,k}$ denote the distance between VLC AP m and OIRS unit k, the distance between vehicle v and OIRS unit k, the irradiance angle of the LED array on VLC AP m, and the incidence angle of the PD on vehicle v, respectively. Based on the location information of APs, OIRSs, and vehicles, the spatial angles $\hat{\varphi}_{k,m}$ and $\hat{\psi}_{v,k}$ can be calculated according to the law of geometry. Besides, F is the reflectivity of the OIRS unit, which depends on the OIRS characteristics.

Based on orthogonal frequency division multiple access (OFDMA), each VLC AP can serve multiple vehicles simultaneously. All optical subchannels are denoted as $\mathcal{L} = \{1, 2, \ldots, L\}$, which are reused among all VLC APs, and each with a bandwidth of W_1. To describe the optical subchannel assignment of VLC AP m, the binary matrix $\boldsymbol{B}_m \in \mathbb{B}^{V\times L}$ is defined, in which $b_{m,v,l} = 1$ indicates the subchannel l of VLC AP m is allocated to vehicle v, while 0 signifies non-allocation. The set of optical subchannel assignment matrices of all VLC APs is denoted as $\mathcal{B} = \{\boldsymbol{B}_m | m \in \mathcal{M}\}$.

Since the size of the OIRS unit is infinitely large compared to the optical wavelength, geometrical optics is suitable for analyzing OIRS reflections. In this case, the power density of the reflected optical beam is concentrated in a small area, ensuring no leakage to other directions [38]. Therefore, the OIRS-reflected link can only be established when the OIRS unit is aligned with the VLC AP and PD. Furthermore, when an OIRS unit is arranged to reflect an optical signal from a VLC AP to a vehicle, the roll and yaw angles of the OIRS unit can be calculated utilizing their locations according to the reflection law. Hence, the problem of configuring OIRS is equivalently transformed into the arrangement of OIRS units. For the arrangement of the m-th OIRS, a binary matrix $\boldsymbol{F}_m$ is defined, and the set of all OIRS arrangement matrices is denoted as $\mathcal{F} = \{\boldsymbol{F}_m | m \in \mathcal{M}\}$. Within $\boldsymbol{F}_m$, the element $f_{m,k,v} = 1$ and 0 signify the unit k of the m-th OIRS is assigned to vehicle v or not, respectively. Meanwhile, the concentrated reflected optical beam ensures no power leakage when $f_{m,k,v} = 0$. Consequently, the total VLC channel gain between VLC AP m and vehicle v is expressed as

$$h_{v,m} = h^{(0)}_{v,m} a_{v,m} + \sum_{k=1}^{K} h^{(1)}_{v,k,m} f_{m,k,v}. \tag{4}$$

B. RF System

The channel gain from the RF AP to vehicle v is modeled by Rayleigh fading [39], [40] as

$$\boldsymbol{g}^{(0)}_v = \sqrt{\rho \hat{u}_{0,v}^{-\alpha_{0,v}}}\, \bar{\boldsymbol{g}}^{(0)}_v, \tag{5}$$

where ρ is the path loss at the reference distance $d_0 = 1$ m. Additionally, $\hat{u}_{0,v}$ and $\alpha_{0,v}$ correspond to the distance and path loss exponent of the link from the RF AP to vehicle v, respectively. The elements of $\bar{\boldsymbol{g}}^{(0)}_v \in \mathbb{C}^{Z\times 1}$ are independent, identically distributed (i.i.d.) in a complex Gaussian distribution with zero mean and unit variance. Moreover, the channel gains from the RF AP to all vehicles are represented as $\boldsymbol{G}^{(0)} = [\boldsymbol{g}^{(0)}_1, \ldots, \boldsymbol{g}^{(0)}_V]^T$.

The channel gains from the RF AP to RF IRS unit n and from RF IRS to vehicle v are modeled by Rician fading [39], [40] as

$$\boldsymbol{g}^{(1)}_n = \sqrt{\rho \hat{u}_1^{-\alpha_1}} \left(\sqrt{\frac{\zeta_1}{1+\zeta_1}} \boldsymbol{g}^{(1)}_{n,\mathrm{LoS}} + \sqrt{\frac{1}{1+\zeta_1}} \boldsymbol{g}^{(1)}_{n,\mathrm{NLoS}} \right), \tag{6}$$

$$\boldsymbol{g}^{(2)}_v = \sqrt{\rho \hat{u}_{2,v}^{-\alpha_{2,v}}} \left(\sqrt{\frac{\zeta_2}{1+\zeta_2}} \boldsymbol{g}^{(2)}_{v,\mathrm{LoS}} + \sqrt{\frac{1}{1+\zeta_2}} \boldsymbol{g}^{(2)}_{v,\mathrm{NLoS}} \right), \tag{7}$$

where α_1 and $\alpha_{2,v}$ represent the path loss exponent of corresponding links, while $\hat{u}_1$ and $\hat{u}_{2,v}$ denote the distances from RF AP to RF IRS and from RF IRS to vehicle v, respectively. The elements of NLoS components $\boldsymbol{g}^{(1)}_{n,\mathrm{NLoS}} \in \mathbb{C}^{Z\times 1}$ and $\boldsymbol{g}^{(2)}_{v,\mathrm{NLoS}} \in \mathbb{C}^{N\times 1}$ follow a complex Gaussian distribution with zero mean and unit variance. Besides, the LoS components $\boldsymbol{g}^{(1)}_{n,\mathrm{LoS}} \in \mathbb{C}^{Z\times 1}$ and $\boldsymbol{g}^{(2)}_{v,\mathrm{LoS}} \in \mathbb{C}^{N\times 1}$ consist of ULA response [39]. The channel gains from RF AP to RF IRS and from RF IRS to all vehicles are denoted as $\boldsymbol{G}^{(1)} = [\boldsymbol{g}^{(1)}_1, \ldots, \boldsymbol{g}^{(1)}_N]^T$ and $\boldsymbol{G}^{(2)} = [\boldsymbol{g}^{(2)}_1, \ldots, \boldsymbol{g}^{(2)}_V]^T$, respectively.

The phase shifts introduced by RF IRS are denoted by a matrix $\boldsymbol{\Phi} = \mathrm{diag}(\phi_1, \ldots, \phi_N)$, where $\phi_n = e^{j\theta_n}$, $n \in \{1, 2, \ldots, N\}$. The phase vector is presented by $\boldsymbol{\theta} = [\theta_1, \theta_2, \ldots, \theta_N]^T$. Subsequently, the total channel gains from the RF AP to all vehicles are expressed as

$$\boldsymbol{G} = \boldsymbol{G}^{(2)} \boldsymbol{\Phi} \boldsymbol{G}^{(1)} + \boldsymbol{G}^{(0)} = \sum_{n=1}^{N} \phi_n \boldsymbol{G}^{(2)} \boldsymbol{\Psi}_n \boldsymbol{G}^{(1)} + \boldsymbol{G}^{(0)}, \tag{8}$$

where $\boldsymbol{\Psi}_n$ is a zero matrix with n-th diagonal element of 1.

III. Problem Formulation for EE Maximization

In the VLC system, the power allocation is given by $\boldsymbol{P} \in \mathbb{R}^{M\times L}$, where $p_{m,l}$ signifies the power allocated to subchannel l of VLC AP m. Notably, when an OIRS unit is arranged to establish a reflective channel between a VLC AP and a vehicle, the optical signal from another VLC AP is reflected towards a different direction. However, the probability of any PD happening to appear exactly in that direction is quite low and can be ignored, thereby causing no interference to other vehicles [31]. Hence, the optical interference received by vehicle v originates from the LoS channels of other VLC APs. Consequently, the SINR on subchannel l from VLC AP m to vehicle v is demonstrated as

$$\gamma_{m,v,l} = \frac{h^2_{v,m} p_{m,l}}{\sum_{m'=1}^{M} (h^{(0)}_{v,m'})^2 p_{m',l} \left(1 - a_{v,m'}\right) + \mu_1 W_1}, \tag{9}$$

where μ_1 is the power spectral density (PSD) of the noise for VLC. For vehicle v served by VLC AP m, it receives the interference from the other VLC APs $m' \neq m$, as indicated by the first term in the denominator of (9). If $m' = m$, then $a_{v,m'} = 1$ holds, and the term corresponding to m in the summation is set to zero. Subsequently, the corresponding achievable data rate for vehicle v via VLC is given by

$$R_{m,v,l} = \frac{W_1}{2} \log_2 \left(1 + \frac{e}{2\pi} \gamma_{m,v,l}\right). \tag{10}$$

Following that, the total achievable data rate of the VLC system received by vehicle v is presented as

$$R_v = \sum_{m=1}^{M} \sum_{l=1}^{L} b_{m,v,l} R_{m,v,l}. \tag{11}$$

For the RF communication system, the power received by each vehicle is represented by $\boldsymbol{q} = [q_1, \ldots, q_V]^T$, which can be organized as a matrix $\boldsymbol{Q} = \mathrm{diag}(\boldsymbol{q})$. Assuming the utilization of zero-forcing (ZF) at the RF AP, the precoding matrix $\boldsymbol{E} \in \mathbb{C}^{Z\times V}$ is given by

$$\boldsymbol{E} = \boldsymbol{G}^{\dagger} = \boldsymbol{G}^H \left(\boldsymbol{G}\boldsymbol{G}^H\right)^{-1}. \tag{12}$$

The precoding vector of vehicle v is denoted as $\boldsymbol{e}_v$, corresponding to the v-th column of $\boldsymbol{E}$. Based on ZF, the achievable data rate via RF received by vehicle v is expressed as

$$S_v = W_2 \log_2 \left(1 + \frac{q_v}{\mu_2 W_2}\right), \tag{13}$$

where μ_2 and W_2 are the PSD of the noise and the bandwidth of RF, respectively. Consequently, the achievable data rate of the IRS-assisted aggregated system is given by

$$R_T = \sum_{v=1}^{V} \left(R_v + S_v\right). \tag{14}$$

Considering the power consumption of the RF AP is $\mathrm{tr}\left(\boldsymbol{EQE}^H\right)$, the total power consumption is denoted by

$$P_T = \sum_{m=1}^{M} \sum_{l=1}^{L} p_{m,l} + \mathrm{tr}\left(\boldsymbol{EQE}^H\right) + U_T, \tag{15}$$

where $U_T = MU_1 + U_2 + NU_3 + MKU_4$ represents the static power consumption of all hardware components. Specifically, U_1, U_2, U_3, and U_4 are hardware static power consumptions of a VLC AP, the RF AP, a unit of RF IRS, and a unit of OIRS, respectively. Consequently, the EE maximization problem of the whole aggregated VLC-RF system is formulated as

$$\text{(P0)} \quad \max_{\mathcal{F},\mathcal{B},\boldsymbol{P},\boldsymbol{Q},\boldsymbol{\Phi}} \eta = \frac{R_T}{P_T} \tag{16}$$

$$\text{s.t.} \quad p_{m,l} \geq 0, \ \ \forall m \in \mathcal{M}, \ \ \forall l \in \mathcal{L}, \tag{16a}$$

$$\sum_{l=1}^{L} p_{m,l} \leq p_{m,\max}, \ \ \forall m \in \mathcal{M}, \tag{16b}$$

$$q_v \geq 0, \ \ \forall v \in \mathcal{V}, \tag{16c}$$

$$\mathrm{tr}\left(\boldsymbol{EQE}^H\right) \leq q_{\max}, \tag{16d}$$

$$\sum_{m=1}^{M} \sum_{l=1}^{L} p_{m,l} + \mathrm{tr}\left(\boldsymbol{EQE}^H\right) + U_T \leq U_{\max}, \tag{16e}$$

$$f_{m,k,v} \in \{0,1\}, \ \ \forall m \in \mathcal{M}, \ \forall k \in \mathcal{K}, \ \forall v \in \mathcal{V}, \tag{16f}$$

$$\sum_{v=1}^{V} f_{m,k,v} \leq 1, \ \ \forall m \in \mathcal{M}, \ \forall k \in \mathcal{K}, \tag{16g}$$

$$f_{m,k,v}\left(1 - a_{v,m}\right) = 0, \ \ \forall m \in \mathcal{M}, \ \forall k \in \mathcal{K}, \ \forall v \in \mathcal{V}, \tag{16h}$$

$$|\phi_n| = 1, \ \ \forall n \in \mathcal{N}, \tag{16i}$$

$$b_{m,v,l} \in \{0,1\}, \ \ \forall m \in \mathcal{M}, \ \forall v \in \mathcal{V}, \ \forall l \in \mathcal{L}, \tag{16j}$$

$$\sum_{v=1}^{V} b_{m,v,l} \leq 1, \ \ \forall m \in \mathcal{M}, \ \forall l \in \mathcal{L}, \tag{16k}$$

$$b_{m,v,l}\left(1 - a_{v,m}\right) = 0, \ \ \forall m \in \mathcal{M}, \ \forall v \in \mathcal{V}, \ \forall l \in \mathcal{L}, \tag{16l}$$

$$R_v + S_v \geq R_{\min}, \ \ \forall v \in \mathcal{V}. \tag{16m}$$

The constraints in the problem (P0) are explained as follows.

Power Allocation Constraints: Constraints (16a) and (16c) ensure the non-negative power allocation for VLC and RF systems, respectively. For both VLC APs and the RF AP, the transmitted powers must not exceed the maximum feasible power of the corresponding AP, which are guaranteed by (16b) and (16d), where $p_{m,\max}$ and $q_{\max}$ are the maximum feasible power for VLC AP m and the RF AP, respectively. To guarantee the power consumption of the aggregated system below the power threshold $U_{\max}$, the total power constraint is formulated as (16e).

OIRS Arrangement Constraints: Constraints (16f), (16g), and (16h) ensure that each element of $\boldsymbol{F}_m$ is a binary value and an OIRS unit is only assigned to no more than one vehicle served by the corresponding VLC AP.

RF IRS Configuration Constraints: Because the RF IRS only adjusts the phase of the signal, the phase shift constraint is formulated as (16i).

Optical Subchannel Assignment Constraints: For an optical subchannel assignment matrix $\boldsymbol{B}_m$, constraints (16j), (16k), and (16l) guarantee that each element is binary, and each subchannel can only be assigned to no more than one vehicle served by the corresponding VLC AP.

Date Rate Constraints: To satisfy the quality of service (QoS) requirements of all vehicles, the achievable data rate of each vehicle should be larger than $R_{\min}$, as formulated by (16m).

IV. Proposed Resource Allocation Algorithm

The problem (P0) falls into the category of mixed integer nonlinear programming (MINLP) problem, a typically intractable issue proven to be a non-deterministic polynomial (NP)-hard problem [41]. In this section, a BCD-based resource allocation algorithm is proposed, which decomposes the problem (P0) into four more solvable subproblems, focusing on RF IRS configuration, optical subchannel assignment, OIRS arrangement, and joint power allocation, respectively. When solving a specific subproblem, some variables are optimized when the remaining variables are fixed, as shown in **Algorithm 1**. In each iteration, RF IRS configuration is solved first by the GD approach, as detailed in Section IV-A. Then, optical subchannel assignment is optimized by the LRH method in Section IV-B, followed by MM-based OIRS arrangement in Section IV-C. Afterwards, joint power allocation is solved by Dinkelbach-based SFP, as shown in Section IV-D. The above process is repeated until the algorithm converges. In addition, the initial point of **Algorithm 1** is selected as a feasible solution for the problem (P0). When solving subproblems alternately, the initial point for each subproblem is the optimization result from the previous iteration, ensuring the availability of a feasible solution for each subproblem. Moreover, since the specific form of IRS has no effect on the above problem formulation, the proposed BCD-based algorithm is also feasible for the system with IRS in the form of either ULA or uniform planar array.

A. RF IRS Configuration

With fixed $\mathcal{F}$, $\mathcal{B}$, $\boldsymbol{P}$, and $\boldsymbol{Q}$, the total achievable data rate R_T becomes a constant value according to (11) and (13), and

Algorithm 1 BCD-Based Resource Allocation Algorithm

1: **Input**: $\boldsymbol{A}$, $\{h_{v,m}^{(0)}\}$, $\{h_{v,k,m}^{(1)}\}$, $\boldsymbol{G}^{(2)}$, $\boldsymbol{G}^{(1)}$, $\boldsymbol{G}^{(0)}$, and the error threshold $\varepsilon_1 > 0$.
2: **Initialization**: $i = 0$, $\mathcal{F}^{(0)}$, $\mathcal{B}^{(0)}$, $\boldsymbol{\Phi}^{(0)}$, $\boldsymbol{P}^{(0)}$, and $\boldsymbol{Q}^{(0)}$ are initialized.
3: **repeat**
4: $i = i + 1$;
5: Given $\mathcal{F}^{(i-1)}$, $\mathcal{B}^{(i-1)}$, $\boldsymbol{P}^{(i-1)}$, and $\boldsymbol{Q}^{(i-1)}$, optimize $\boldsymbol{\Phi}^{(i)}$ by GD approach;
6: Given $\boldsymbol{\Phi}^{(i)}$, $\mathcal{F}^{(i-1)}$, $\boldsymbol{P}^{(i-1)}$, and $\boldsymbol{Q}^{(i-1)}$, optimize $\mathcal{B}^{(i)}$ by LRH method;
7: Given $\boldsymbol{\Phi}^{(i)}$, $\mathcal{B}^{(i)}$, $\boldsymbol{P}^{(i-1)}$, and $\boldsymbol{Q}^{(i-1)}$, optimize $\mathcal{F}^{(i)}$ by MM method;
8: Given $\boldsymbol{\Phi}^{(i)}$, $\mathcal{B}^{(i)}$, and $\mathcal{F}^{(i)}$, optimize $\boldsymbol{P}^{(i)}$, and $\boldsymbol{Q}^{(i)}$ by Dinkelbach-based SFP;
9: **until** $|\eta^{(i)} - \eta^{(i-1)}| < \varepsilon_1$
10: **Output**: $\boldsymbol{\Phi}^{(i)}$, $\mathcal{B}^{(i)}$, $\mathcal{F}^{(i)}$, $\boldsymbol{P}^{(i)}$, and $\boldsymbol{Q}^{(i)}$

thus the problem (P0) is transformed into minimizing the total power consumption as

$$\text{(P1)} \quad \min_{\boldsymbol{\theta}} \ \Gamma_1(\boldsymbol{\theta}) = \operatorname{tr}\left(\boldsymbol{E}\boldsymbol{Q}\boldsymbol{E}^H\right) \quad \text{s.t.} \quad (16d), (16e). \tag{17}$$

If the minimum value of $\Gamma_1(\boldsymbol{\theta})$ is obtained and satisfies the constraints (16d) and (16e), the problem (P1) is solved. Moreover, the GD approach is employed to minimize $\Gamma_1(\boldsymbol{\theta})$, and the gradient is calculated based on Lemma 1.

Lemma 1: *The partial derivative of $\Gamma_1(\boldsymbol{\theta})$ with respect to θ_n is given by*

$$\frac{\partial \Gamma_1(\boldsymbol{\theta})}{\partial \theta_n} = -2\text{Re}\left\{je^{j\theta_n}\operatorname{tr}\left(\boldsymbol{G}^H\hat{\boldsymbol{G}}\tilde{\boldsymbol{G}}_n\right)\right\}, \tag{18}$$

where $\hat{\boldsymbol{G}} = \left(\boldsymbol{G}\boldsymbol{G}^H\right)^{-1}\boldsymbol{Q}\left(\boldsymbol{G}\boldsymbol{G}^H\right)^{-1}$ is a Hermitian matrix and $\tilde{\boldsymbol{G}}_n = \boldsymbol{G}^{(2)}\boldsymbol{\Psi}_n\boldsymbol{G}^{(1)}$.

Proof: The proof is presented in Appendix A. □

Subsequently, the gradient of $\Gamma_1(\boldsymbol{\theta})$ is given by

$$\nabla_{\boldsymbol{\theta}}\Gamma_1(\boldsymbol{\theta}) = \left[\frac{\partial \Gamma_1(\boldsymbol{\theta})}{\partial \theta_1}, \frac{\partial \Gamma_1(\boldsymbol{\theta})}{\partial \theta_2}, \ldots, \frac{\partial \Gamma_1(\boldsymbol{\theta})}{\partial \theta_N}\right]^T. \tag{19}$$

To sum up, the GD-based RF IRS configuration algorithm is summarized in **Algorithm 2**.

B. Optical Subchannel Assignment

For fixed $\mathcal{F}$, $\boldsymbol{\Phi}$, $\boldsymbol{P}$, and $\boldsymbol{Q}$, the total power consumption P_T and the achievable data rate S_v become constant values, and thus the problem (P0) can be simplified to

$$\text{(P2)} \quad \max_{\mathcal{B}} \ \Gamma_2(\mathcal{B}) = \sum_{v=1}^{V} R_v(\mathcal{B}) \quad \text{s.t.} \quad (16j), (16k), (16l), (16m). \tag{20}$$

To solve the problem (P2), the property of $\Gamma_2(\mathcal{B})$ needs to be studied first, which is given in Lemma 2.

Algorithm 2 GD-Based RF IRS Configuration Algorithm

1: **Input**: $\boldsymbol{Q}, \boldsymbol{G}^{(2)}, \boldsymbol{G}^{(1)}, \boldsymbol{G}^{(0)}$, and the error threshold $\varepsilon_2 > 0$.
2: **Initialization**: $\tau = 0$, and $\boldsymbol{\theta}^{(0)}$ is initialized.
3: **repeat**
4: Calculate $\nabla_{\boldsymbol{\theta}}\Gamma_1\left(\boldsymbol{\theta}^{(\tau)}\right)$ based on (18) and (19);
5: Calculate the stepsize μ_τ by backtracking line search;
6: $\boldsymbol{\theta}^{(\tau+1)} = \boldsymbol{\theta}^{(\tau)} - \mu_\tau \nabla_{\boldsymbol{\theta}}\Gamma_1\left(\boldsymbol{\theta}^{(\tau)}\right)$;
7: $\boldsymbol{\theta}^{(\tau+1)} = \boldsymbol{\theta}^{(\tau+1)} - 2\pi\lfloor\frac{\boldsymbol{\theta}^{(\tau+1)}}{2\pi}\rfloor$;
8: $\tau = \tau + 1$;
9: **until** $\left|\Gamma_1\left(\boldsymbol{\theta}^{(\tau)}\right) - \Gamma_1\left(\boldsymbol{\theta}^{(\tau-1)}\right)\right| < \varepsilon_2$
10: **Output**: $\boldsymbol{\theta}^* = \boldsymbol{\theta}^{(\tau)}$

Lemma 2: *$\Gamma_2(\mathcal{B})$ is a non-decreasing function of $b_{m,v,l}$.*

Proof: Considering (10), (11), and (20) comprehensively, $\Gamma_2(\mathcal{B})$ is a linear function of $b_{m,v,l}$ with the non-negative coefficient $R_{m,v,l}$. Therefore, Lemma 2 is proved. □

Based on Lemma 2, the optimal result of problem (P2) is obtained at the boundary of (16k), which is transformed into

$$\sum_{v\in\mathcal{V}} b_{m,v,l} = 1, \quad \forall m \in \mathcal{M}, \ \forall l \in \mathcal{L}. \tag{21}$$

Since the subchannels of a VLC AP are only assigned to vehicles it serves, the elements of $\boldsymbol{B}_m$ satisfy $b_{m,v,l} = 0$ $(v \notin \mathcal{V}_m)$, which are deterministic without optimization. Consequently, the remaining optimization variables form a matrix $\hat{\boldsymbol{B}}_m \in \mathbb{B}^{V_m \times L}$. In addition, for any vehicle $v \in \mathcal{V}_m$, the condition $a_{v,m} = 1$ is guaranteed, and thus (16l) is satisfied and then omitted. Moreover, since each vehicle is served by only one VLC AP, the problem (P2) is decomposed into M subproblems to accomplish the optical subchannel assignment for each VLC AP separately, and these subproblems are in the same form as

$$\text{(P2-1)} \quad \max_{\hat{\boldsymbol{B}}_m} \ \Gamma_{2m}(\hat{\boldsymbol{B}}_m) = \sum_{v\in\mathcal{V}_m} R_v(\hat{\boldsymbol{B}}_m), \ \forall m \in \mathcal{M} \quad \text{s.t.} \quad (16j), (21), (16m). \tag{22}$$

The problem (P2-1) is a generalized assignment problem (GAP), which is a well-established NP-hard problem [42]. In this paper, the Lagrangian relaxation (LR) method is employed to solve the problem (P2-1). To decrease the complexity of the problem (P2-1), the data rate constraint is relaxed into the object function as

$$\hat{\Gamma}_{2m}(\hat{\boldsymbol{B}}_m) = \sum_{v\in\mathcal{V}_m} R_v + \varpi_v\left(R_v + S_v - R_{\min}\right), \tag{23}$$

where $\varpi_v \geq 0$ is a Lagrangian multiplier and $\boldsymbol{\varpi}_m = [\varpi_1, \ldots, \varpi_{V_m}]$. Then, the problem (P2-1) is transformed into

$$\text{(P2-2)} \quad \max_{\hat{\boldsymbol{B}}_m} \ \hat{\Gamma}_{2m}(\hat{\boldsymbol{B}}_m), \ \forall m \in \mathcal{M} \quad \text{s.t.} \quad (16j), (21). \tag{24}$$

For fixed $\boldsymbol{\varpi}_m$, the optimal solution of the problem (P2-2) is given by

$$b_{m,v,l} = \begin{cases} 1, & v = \arg\max_{v'} \left(\varpi_{v'} + 1\right) R_{m,v',l}, \\ 0, & \text{otherwise}. \end{cases} \tag{25}$$

Based on subchannel assignment in (25) obtained by the LR method, an upperbound of the problem (P2-1) is attained. To obtain a tighter upperbound, the subgradient method is employed to update the Lagrangian multipliers, and the subgradient is given by $\boldsymbol{J}_m = [J_m(\varpi_1), \ldots, J_m(\varpi_{V_m})]$, where

$$J_m(\varpi_v) = -\sum_{l \in \mathcal{L}} R_{m,v,l} b_{m,v,l} - S_v + R_{\min}, \ \ \forall v \in \mathcal{V}_m. \tag{26}$$

Then, the update of the Lagrangian multipliers is given by

$$\varpi_v^{(\tau+1)} = \max\left\{0, \varpi_v^{(\tau)} + \Omega \frac{\aleph - \gimel}{\|\boldsymbol{J_m}\|_2^2} J_m(\varpi_v)\right\}, \ \forall v \in \mathcal{V}_m, \tag{27}$$

where τ, $\aleph$, and $\gimel$ represent the iteration number, the upperbound, and the lowerbound of $\hat{\Gamma}_{2m}$, respectively. Besides, Ω denotes the control parameter that satisfies $0 \le \Omega \le 2$ [43].

Due to the relaxed data rate constraint, the solution acquired by LR is not always a feasible solution for the problem (P2-1). As a consequence, a heuristics approach is utilized to reconstruct a feasible solution close to (25), in which some subchannels are reassigned from constraint-satisfied vehicles to constraint-unsatisfied vehicles so that all constraints of the original problem are finally satisfied, as shown in **Steps** 9∼20 of **Algorithm 3**. Specifically, the vehicles served by VLC AP m, whose data rate constraints are not satisfied, constitute the set $\hat{\mathcal{V}}_m$. For each vehicle $\hat{v} \in \hat{\mathcal{V}}_m$, some subchannels assigned to vehicle $v' \in \mathcal{V}_m - \hat{\mathcal{V}}_m$ are reassigned to $\hat{v}$ if this transfer does not violate the data rate constraint of v'. To sum up, the above LRH-based subchannel assignment is illustrated in **Algorithm 3**.

Algorithm 3 LRH-Based Optical Subchannel Assignment Algorithm

1: **Input**: $\boldsymbol{A}, \boldsymbol{P}, \boldsymbol{Q}, \{h_{v,m}^{(0)}\}, \{h_{v,k,m}^{(1)}\}$, and $\mathcal{F}$.
2: **Initialization**: $m = 1$, $\tau = 0$, $\gimel = -\infty$, $\aleph = \infty$, $\tau_{\max}$, and $\varpi_v^{(0)}$ are initialized.
3: **repeat**
4: Compute $\{R_{m,v,l}\}_{v \in \mathcal{V}_m, l \in \mathcal{L}}$ based on (10);
5: **repeat**
6: Obtain subchannel assignment $\hat{\boldsymbol{B}}_m$ based on (25);
7: The upperbound $\aleph = \min\{\aleph, \hat{\Gamma}_{2m}(\hat{\boldsymbol{B}}_m)\}$;
8: Compute $\boldsymbol{J}_m$ based on (26);
9: $\hat{\mathcal{V}}_m = \{v | R_v + S_v - R_{\min} < 0, v \in \mathcal{V}_m\}$;
10: **for** $\hat{v} \in \hat{\mathcal{V}}_m$ **do**
11: $\hat{\mathcal{L}}_{m,\hat{v}}^{(\tau)} = \{l | b_{m,\hat{v},l} = 0\}$;
12: **repeat**
13: $l' = \arg\max\{R_{m,\hat{v},l} | \ l \in \hat{\mathcal{L}}_{m,\hat{v}}^{(\tau)}\}$;
14: $v' = \{v | \ b_{m,v,l'} = 1\}$;
15: **if** $R_{v'} - R_{m,v',l'} + S_{v'} - R_{\min} \ge 0$ **then**
16: $b_{m,v',l'} = 0$, $b_{m,\hat{v},l'} = 1$;
17: **end if**
18: $\hat{\mathcal{L}}_{m,\hat{v}}^{(\tau)} = \hat{\mathcal{L}}_{m,\hat{v}}^{(\tau)} - \{l'\}$;
19: **until** $R_{\hat{v}} + S_{\hat{v}} - R_{\min} \ge 0$.
20: **end for**
21: The lowerbound $\gimel = \max\{\gimel, \Gamma_{2m}(\hat{\boldsymbol{B}}_m)\}$;
22: Update $\boldsymbol{\varpi}_m^{(\tau+1)}$ according to (27), $\tau = \tau + 1$;
23: **until** $|\aleph - \gimel| < 1$ or $\tau \ge \tau_{\max}$.
24: $m = m + 1$, $\tau = 0$, $\gimel = -\infty$, $\aleph = \infty$;
25: **until** $m > M$
26: **Output**: $\{\hat{\boldsymbol{B}}_m^*\}_{m=1}^M$

C. OIRS Arrangement

Given fixed $\boldsymbol{\Phi}$, $\mathcal{B}$, $\boldsymbol{P}$, and $\boldsymbol{Q}$, the power consumption P_T and the achievable data rate via RF S_v become constant values, and thus the problem (P0) can be simplified to

$$\text{(P3)} \ \ \max_{\mathcal{F}} \ \ \Gamma_3(\mathcal{F}) = \sum_{v=1}^{V} R_v(\mathcal{F}) \tag{28}$$
$$\text{s.t.} \ \ \text{(16f)}, \text{(16g)}, \text{(16h)}, \text{(16m)}.$$

To solve the problem (P3), the property of $\Gamma_3(\mathcal{F})$ is discussed first in Lemma 3.

Lemma 3: *$\Gamma_3(\mathcal{F})$ is a non-decreasing function of $f_{m,k,v}$.*

Proof: Due to the non-negativity of $h_{v,k,m}^{(1)}$ and linearity of (4), $h_{v,m}$ is a non-negative and non-decreasing function of $f_{m,k,v}$. In the value range of $h_{v,m}$, $\gamma_{m,v,l}(h_{v,m})$ is an increasing function of $h_{v,m}$. Besides, $R_v(\gamma_{m,v,l})$ is an increasing function of $\gamma_{m,v,l}$. Therefore, $R_v(\mathcal{F})$ is a non-decreasing function of $f_{m,k,v}$ because it is a compound function of the above functions. □

Based on Lemma 3, the optimal solution for problem (P3) is obtained at the boundary of (16g), which is transformed into

$$\sum_{v \in \mathcal{V}} f_{m,k,v} = 1, \ \ \forall m \in \mathcal{M}, \ \forall k \in \mathcal{K}. \tag{29}$$

Due to constraint (16f), the problem (P3) is an integer programming problem, known to be NP-hard [44]. Consequently, exhaustive search and the branch-and-bound method emerge as viable approaches for optimal solution discovery. However, the complexity of the exhaustive search increases exponentially with the number of optimization variables. Although the branch-and-bound method mitigates the exhaustive search complexity, it remains exponential in the worst case. Therefore, an OIRS arrangement algorithm with low complexity is proposed as follows. First, constraint (16f) is relaxed to

$$0 \le f_{m,k,v} \le 1, \ \ \forall m \in \mathcal{M}, \ \forall K \in \mathcal{K}, \ \forall v \in \mathcal{V}. \tag{30}$$

Considering the non-negativity of $f_{m,k,v}$ and sum constraint of (29), $f_{m,k,v} \le 1$ is guaranteed, and thus (30) is simplified as

$$f_{m,k,v} \ge 0, \ \ \forall m \in \mathcal{M}, \ \forall K \in \mathcal{K}, \ \forall v \in \mathcal{V}. \tag{31}$$

Since each OIRS is only allocated to a vehicle served by the corresponding VLC AP, the elements in $\boldsymbol{F}_m$ satisfy $f_{m,k,v} = 0 \ (v \notin \mathcal{V}_m)$, and thus only $\{f_{m,k,v} | \ v \in \mathcal{V}_m\}$ need to be optimized. The optimized variables can be reduced to

$\hat{\boldsymbol{F}}_m \in \mathbb{R}^{K\times V_m}$, with its vectorization and the v-th column denoted as $\hat{\boldsymbol{f}}_m = \mathrm{vec}(\hat{\boldsymbol{F}}_m)$ and $\hat{\boldsymbol{f}}_{m,v}$, respectively. Besides, for vehicles $v \in \mathcal{V}_m$, the condition $a_{v,m} = 1$ is guaranteed, and thus (16h) is satisfied and can be omitted.

Furthermore, because a vehicle is served by only one VLC AP, the problem (P3) is decomposed into M subproblems with the same form as

$$\text{(P3-1)} \max_{\hat{\boldsymbol{f}}_m} \ \Gamma_{3m}(\hat{\boldsymbol{f}}_m) = \sum_{v\in\mathcal{V}_m} R_v(\hat{\boldsymbol{f}}_m), \ \forall m \in \mathcal{M} \quad (32)$$
$$\text{s.t.} \quad (29), (31), (16\text{m}).$$

To address the non-convex problem (P3-1), the MM algorithm is employed. By solving a series of approximate convex problems, the solutions of these subproblems converge to the Karush-Kuhn-Tucker (KKT) point of the original problem [45]. To establish the approximate convex problems, a lower bound of the objective function needs to be obtained first. For any non-negative ξ and ξ_0, the inequality $\log_2(1+\xi) \geq r\log_2(\xi) + s$ holds with coefficients of

$$r = \frac{\xi_0}{1+\xi_0}, \quad (33)$$
$$s = \log_2(1+\xi_0) - r\log_2 \xi_0, \quad (34)$$

and the inequality is tight for $\xi = \xi_0$ [46]. Subsequently, a lowerbound of R_v is given by

$$\underline{R}_v = \sum_{m=1}^{M}\sum_{l=1}^{L} b_{m,v,l}\frac{W_1}{2}\left[r_{m,v,l}\log_2\left(\frac{e}{2\pi}\gamma_{m,v,l}\right) + s_{m,v,l}\right]. \quad (35)$$

The coefficients in the τ-th loop are expressed as

$$r_{m,v,l}^{(\tau)} = \frac{\frac{e}{2\pi}\gamma_{m,v,l}^{(\tau)}}{1+\frac{e}{2\pi}\gamma_{m,v,l}^{(\tau)}}, \quad (36)$$
$$s_{m,v,l}^{(\tau)} = \log_2\left(1+\frac{e}{2\pi}\gamma_{m,v,l}^{(\tau)}\right) - r_{m,v,l}^{(\tau)}\log_2\left(\frac{e}{2\pi}\gamma_{m,v,l}^{(\tau)}\right), \quad (37)$$

where $\gamma_{m,v,l}^{(\tau)}$ is the SINR on subchannel l from VLC AP m to vehicle v in the τ-th loop. The concavity of $\underline{R}_v$ is proved in Lemma 4.

Lemma 4: *For $v \in \mathcal{V}_m$, $\underline{R}_v(\hat{\boldsymbol{f}}_m)$ is a concave function.*

proof: The proof is given in Appendix B. □

Considering the requirements of the MM algorithm, a lowerbound of $\Gamma_{3m}(\hat{\boldsymbol{f}}_m)$ is adopted as the optimization object, and the problem (P3-1) is approximated by

$$\text{(P3-2)} \ \max_{\hat{\boldsymbol{f}}_m} \ \underline{\Gamma}_{3m}(\hat{\boldsymbol{f}}_m) = \sum_{v\in\mathcal{V}_m} \underline{R}_v(\hat{\boldsymbol{f}}_m), \ \forall m \in \mathcal{M} \quad (38)$$
$$\text{s.t.} \quad (29), (31),$$
$$\underline{R}_v \geq R_{\min} - S_v, \ \ \forall v \in \mathcal{V}_m. \quad (39)$$

Consequently, its convexity is explored in Proposition 1.

Proposition 1: *The problem (P3-2) is a convex problem.*

Proof: The objective function, $\underline{\Gamma}_{3m}(\hat{\boldsymbol{f}}_m)$, demonstrates concavity as it is composed of several individual concave functions. The constraint (39) is a convex constraint according to the Lemma 4. In addition, the constraints (29) and (31) are affine. Hence, the problem (P3-2) is convex. □

Algorithm 4 MM-Based OIRS Arrangement Algorithm

1: **Input**: $\boldsymbol{A}, \boldsymbol{P}, \boldsymbol{Q}, \{h_{v,m}^{(0)}\}, \{h_{v,k,m}^{(1)}\}, \mathcal{B}$, and the error threshold $\varepsilon_4 > 0$.
2: **Initialization**: $m=1$, $\tau=0$, $k=1$, and $\{\hat{\boldsymbol{f}}_m^{(0)}\}_{m=1}^{M}$ is initialized.
3: **repeat**
4:   **repeat**
5:     Calculate $\gamma_{m,v,l}(\hat{\boldsymbol{f}}_m^{(\tau)})$, for $\forall v \in \mathcal{V}_m$, and $\forall l \in \mathcal{L}$;
6:     Calculate $r_{m,v,l}^{(\tau)}, s_{m,v,l}^{(\tau)}$ according to (36) and (37);
7:     Solve problem (P3-2) by IPM and obtain $\hat{\boldsymbol{f}}_m^{(\tau+1)}$;
8:     $\tau = \tau + 1$;
9:   **until** $\|\hat{\boldsymbol{f}}_m^{(\tau)} - \hat{\boldsymbol{f}}_m^{(\tau-1)}\|_2 < \varepsilon_4$
10:   $\hat{\boldsymbol{f}}_m^{*} = \hat{\boldsymbol{f}}_m^{(\tau)}$;
11:   **repeat**
12:     $v^* = \arg\max_{v} \hat{f}_{m,k,v}^{*}$;
13:     $\hat{f}_{m,k,v^*}^{*} = 1$ and $\hat{f}_{m,k,v\neq v^*}^{*} = 0$;
14:     $k = k + 1$;
15:   **until** $k > K$
16:   $m = m + 1$, $\tau = 0$, $k = 1$.
17: **until** $m > M$
18: **Output**: $\{\hat{\boldsymbol{f}}_m^{*}\}_{m=1}^{M}$

As illustrated in the inner loop of **Algorithm 4**, the problem (P3-2) is utilized to replace the problem (P3-1), and then solved by the interior point method (IPM). When the stop condition is satisfied, the solution $\hat{\boldsymbol{f}}_m^{*}$ converges to the KKT point of the problem (P3-1). To satisfy the constraint (16f), a greedy approach is adopted in **Steps** 11∼15 of **Algorithm 4**, obtaining a suboptimal solution of the problem (P3).

D. Joint Power Allocation

For fixed $\mathcal{B}$, $\mathcal{F}$, and $\boldsymbol{\Phi}$, the problem (P0) is simplified to

$$\text{(P4)} \ \max_{\boldsymbol{P},\boldsymbol{Q}} \ \eta = \frac{R_T}{P_T} \quad (40)$$
$$\text{s.t.} \ (16a), (16b), (16c), (16d), (16e), (16m).$$

To solve the problem (P4), the SFP is employed by solving a series of approximate problems, whose solutions converge to the KKT point of the original fractional programming problem [47]. To utilize the SFP, a lowerbound of the EE is adopted to replace the object function, and thus the approximate problem is demonstrated as

$$\text{(P4-1)} \ \max_{\boldsymbol{P},\boldsymbol{Q}} \ \Gamma_4(\boldsymbol{P},\boldsymbol{Q}) = \frac{\underline{R}_T}{P_T} = \frac{\sum_{v=1}^{V}(\underline{R}_v + S_v)}{P_T} \quad (41)$$
$$\text{s.t.} \ (16a), (16b), (16c), (16d), (16e),$$
$$\underline{R}_v + S_v \geq R_{\min}, \ \ \forall v \in \mathcal{V}. \quad (42)$$

To further solve the approximate problem, the VLC power allocation is expressed as the exponential function in $p_{m,l} = 2^{c_{m,l}}$, and related variables are defined as $\boldsymbol{c}_l = [c_{1,l},\ldots,c_{M,l}]^T$ and $\boldsymbol{c} = [\boldsymbol{c}_1^T,\ldots,\boldsymbol{c}_L^T]^T$. Besides, the sum of the interference and noise power received by vehicle v is denoted as

$$\varrho_{v,l} = \sum_{m'=1}^{M} (h_{v,m'}^{(0)})^2 2^{c_{m',l}} (1 - a_{v,m'}) + \mu_1 W_1. \tag{43}$$

Following that, the lowerbound of VLC rate $\underline{R}_v(\boldsymbol{c})$ is demonstrated as (44), shown at the bottom of the page. To study the characteristic of $\Gamma_4(\boldsymbol{c}, \boldsymbol{q})$, the property of $\underline{R}_T(\boldsymbol{c}, \boldsymbol{q})$ is represented in Lemma 5.

Lemma 5: *$\underline{R}_T(\boldsymbol{c}, \boldsymbol{q})$ is a concave function.*

Proof: The proof is given in Appendix C. □

Based on Lemma 5, the category of the problem (P4-1) is given in Proposition 2.

Proposition 2: *The problem (P4-1) is a concave-convex fractional programming (CCFP) problem.*

Proof: Since (15) is an exponential summation of $\boldsymbol{c}$ and an affine function of $\boldsymbol{q}$, $P_T(\boldsymbol{c}, \boldsymbol{q})$ is a convex function. According to Lemma 5, the numerator of (41) is a concave function. In addition, constraints (16c), (16d), and (16e) are affine constraints of $\boldsymbol{q}$. On account of the exponential summations of $\boldsymbol{c}$ in (16b) and (16e), both constraints are convex constraints. Additionally, the numerator and the denominator of (41) are non-negative and positive, respectively. □

To solve the CCFP problem (P4-1), the Dinkelbach algorithm tackles a sequence of subproblems with the parameter β, which are demonstrated as

$$\begin{aligned} \text{(P4-2)} \quad & \max_{\boldsymbol{c},\boldsymbol{q}} \ \Xi_\beta(\boldsymbol{c}, \boldsymbol{q}) = \underline{R}_T - \beta P_T \\ & \text{s.t.} \ (16b), (16c), (16d), (16e), (42). \end{aligned} \tag{45}$$

According to Proposition 2, it is easy to prove that the problem (P4-2) is a convex optimization problem. In each outer loop of **Algorithm 5**, the problem (P4) is replaced by the problem (P4-1), and then transformed into the problem (P4-2) in the inner loop, which is solved by the Dinkelbach algorithm. When the stop condition of the inner loop is satisfied, the optimization variables converge to the global optimal solution of the problem (P4-1) [48]. When the stop condition of the outer loop is satisfied, the solution converges to the KKT point of the problem (P4).

E. Analysis of Convergence and Complexity

In order to analyze the convergence of the proposed BCD-based resource allocation algorithm, the convergences of algorithms solving the four subproblems are analyzed first.

For the problem (P1), the non-decreasing of the object function is guaranteed by the properties of GD and the backtracking line search, which is demonstrated as $\Gamma_1(\boldsymbol{\Phi}^{(i)}) \leq \Gamma_1(\boldsymbol{\Phi}^{(i-1)})$.

In the subchannel assignment subproblem, $\boldsymbol{B}_m^{(i)}$ is given by

$$\boldsymbol{B}_m^{(i)} = \arg\max_{\boldsymbol{B}_m} (\Gamma_2(\boldsymbol{B}_m^{(i-1)}), \Gamma_2(\boldsymbol{B}_m^*)), \tag{46}$$

Algorithm 5 Dinkelbach-Based SFP Joint Power Allocation Algorithm

Input: $\boldsymbol{A}$, $\{h_{v,m}^{(0)}\}$, $\{h_{v,k,m}^{(1)}\}$, $\mathcal{F}$, $\mathcal{B}$, $\boldsymbol{\Phi}$, $\boldsymbol{G}^{(2)}$, $\boldsymbol{G}^{(1)}$, $\boldsymbol{G}^{(0)}$, and the error threshold $\varepsilon_5, \varepsilon_6 > 0$.
Initialization: $\tau = 0$, $\iota = 0$, $\beta^{(\tau,\iota)} = 0$, $\boldsymbol{c}^{(\tau,\iota)}$, and $\boldsymbol{q}^{(\tau,\iota)}$ are initialized.
repeat
  Calculate $\gamma_{m,v,l}^{(\tau)}$ for $\forall m \in \mathcal{M}, \forall v \in \mathcal{V}, \forall l \in \mathcal{L}$ based on $\boldsymbol{c}^{(\tau,0)}$ and $\boldsymbol{q}^{(\tau,0)}$;
  Calculate $r_{m,v,l}^{(\tau)}, s_{m,v,l}^{(\tau)}$ according to (36) and (37);
  repeat
    $\iota = \iota + 1$;
    Solve the problem (P4-2) by IPM and obtain $\boldsymbol{c}^{(\tau,\iota)}, \boldsymbol{q}^{(\tau,\iota)}$;
    Calculate $\Xi_{\beta^{(\tau,\iota-1)}}(\boldsymbol{c}^{(\tau,\iota)}, \boldsymbol{q}^{(\tau,\iota)})$ based on (45);
    $\beta^{(\tau,\iota)} = \underline{R}_T(\boldsymbol{c}^{(\tau,\iota)}, \boldsymbol{q}^{(\tau,\iota)}) / P_T(\boldsymbol{c}^{(\tau,\iota)}, \boldsymbol{q}^{(\tau,\iota)})$;
  until $\Xi_{\beta^{(\tau,\iota-1)}}(\boldsymbol{c}^{(\tau,\iota)}, \boldsymbol{q}^{(\tau,\iota)}) < \varepsilon_5$;
  $\boldsymbol{c}^{(\tau+1,0)} = \boldsymbol{c}^{(\tau,\iota)}, \boldsymbol{q}^{(\tau+1,0)} = \boldsymbol{q}^{(\tau,\iota)}$;
  $\tau = \tau + 1, \iota = 0$, $\beta^{(\tau,\iota)} = 0$;
until $|\eta(\boldsymbol{c}^{(\tau,0)}, \boldsymbol{q}^{(\tau,0)}) - \eta(\boldsymbol{c}^{(\tau-1,0)}, \boldsymbol{q}^{(\tau-1,0)})| < \varepsilon_6$
Output: $\boldsymbol{c}^* = \boldsymbol{c}^{(\tau,0)}, \boldsymbol{q}^* = \boldsymbol{q}^{(\tau,0)}$

where $\boldsymbol{B}_m^*$ is the output of **Algorithm 3**. Hence, $\Gamma_2(\boldsymbol{B}_m^{(i)}) \geq \Gamma_2(\boldsymbol{B}_m^{(i-1)})$ is guaranteed in the i-th loop of **Algorithm 1**.

In the τ-th loop of **Algorithm 4**, it can be shown that

$$\Gamma_{3m}(\hat{\boldsymbol{f}}_m^{(\tau-1)}) = \underline{\Gamma}_{3m}(\hat{\boldsymbol{f}}_m^{(\tau-1)}) \tag{47a}$$
$$\leq \underline{\Gamma}_{3m}(\hat{\boldsymbol{f}}_m^{(\tau)}) \tag{47b}$$
$$\leq \Gamma_{3m}(\hat{\boldsymbol{f}}_m^{(\tau)}). \tag{47c}$$

The equation (47a) holds because $\underline{\Gamma}_{3m}$ is tight with respect to Γ_{3m} at $\hat{\boldsymbol{f}}_m^{(\tau-1)}$ in the τ-th loop. The inequality (47b) is ensured by the IPM optimization process of the problem (P3-2), while (47c) holds because $\underline{\Gamma}_{3m}$ is the lowerbound of Γ_{3m}. In addition, a selection procedure similar to (46) is performed to $\boldsymbol{F}_m$, thereby $\Gamma_3(\boldsymbol{F}_m^{(i)}) \geq \Gamma_3(\boldsymbol{F}_m^{(i-1)})$ holds in the i-th loop of **Algorithm 1**.

Similar to (47a), (47b), and (47c), the non-decreasing property of EE in the outer loop of **Algorithm 5** is formulated by

$$\begin{aligned} \eta(\boldsymbol{P}^{(\tau-1,0)}, \boldsymbol{Q}^{(\tau-1,0)}) &= \Gamma_4(\boldsymbol{P}^{(\tau-1,0)}, \boldsymbol{Q}^{(\tau-1,0)}) \\ &\leq \Gamma_4(\boldsymbol{P}^{(\tau,0)}, \boldsymbol{Q}^{(\tau,0)}) \leq \eta(\boldsymbol{P}^{(\tau,0)}, \boldsymbol{Q}^{(\tau,0)}). \end{aligned} \tag{48}$$

Subsequently, the non-decreasing property $\eta(\boldsymbol{P}^{(i-1)}, \boldsymbol{Q}^{(i-1)}) \leq \eta(\boldsymbol{P}^{(i)}, \boldsymbol{Q}^{(i)})$ is ensured in the i-th loop of **Algorithm 1**.

Based on the above discussions, the non-decreasing property of EE in the i-th iteration of the proposed algorithm is

$$\underline{R}_v(\boldsymbol{c}) = \frac{W_1}{2} \sum_{l=1}^{L} b_{m_v,v,l} \left[r_{m_v,v,l} c_{m_v,l} - r_{m_v,v,l} \log_2(\varrho_{v,l}) + r_{m_v,v,l} \log_2\left(\frac{e h_{v,m_v}^2}{2\pi}\right) + s_{m_v,v,l} \right]. \tag{44}$$

given by

$$\eta(\mathbf{\Phi}^{(i-1)}, \mathcal{B}^{(i-1)}, \mathcal{F}^{(i-1)}, \boldsymbol{P}^{(i-1)}, \boldsymbol{Q}^{(i-1)}) \leq \eta(\mathbf{\Phi}^{(i)}, \mathcal{B}^{(i)}, \mathcal{F}^{(i)}, \boldsymbol{P}^{(i)}, \boldsymbol{Q}^{(i)}). \quad (49)$$

Due to the constraints of the problem (P0), EE is upper-bounded by a finite value, thereby the convergence of the proposed algorithm is guaranteed. Nevertheless, since the objective function is not jointly concave with respect to all optimization variables, the solution obtained by the proposed BCD-based algorithm is a suboptimal solution.

To analyze the computational complexity of the proposed resource allocation method, the complexity of solving each subproblem is discussed first. The iteration numbers of the outer loop in **Algorithm 1** and **Algorithm 2** are denoted as I_1 and I_2, respectively.

For **Algorithm 2**, the computation mainly takes place in the calculation of the $\nabla_{\boldsymbol{\theta}}\Gamma_1(\boldsymbol{\theta})$, which is given by $\mathcal{O}(I_2(NZV + ZV^2 + V^3))$.

For **Algorithm 3**, **Step** 6 leads to $\mathcal{O}(V_m L)$ comparisons, and **Step** 8 results in $\mathcal{O}(V_m L)$ multiplications in τ-th iteration. To facilitate the adjustment of optical subchannel assignment of **Steps** 12∼20, $\{R_{m,\hat{v},l} | l \in \hat{\mathcal{L}}_{m,\hat{v}}^{(\tau)}\}$ are sorted for each $\hat{v} \in \hat{\mathcal{V}}_m$ in τ-th iteration, thereby causing $\mathcal{O}(\sum_{\hat{v}=1}^{|\mathcal{V}_m^{(\tau)}|} |\hat{\mathcal{L}}_{m,\hat{v}}^{(\tau)}| \log(|\hat{\mathcal{L}}_{m,\hat{v}}^{(\tau)}|))$ operations, which is no more than $\mathcal{O}(V_m L \log(L))$. Hence, the total computational complexity of **Algorithm 3** is given by $\mathcal{O}(\sum_{m=1}^{M} \sum_{\tau=1}^{I_{3m}} (V_m L + \sum_{\hat{v}=1}^{|\mathcal{V}_m^{(\tau)}|} |\hat{\mathcal{L}}_{m,\hat{v}}^{(\tau)}| \log(|\hat{\mathcal{L}}_{m,\hat{v}}^{(\tau)}|)))$, where I_{3m} is the iteration number for the problem (P2-1).

In **Algorithm 4**, the problem (P3-2) can be solved by IPM with the complexity of $\mathcal{O}((KV_m)^{3.5} \log_2(1/\hat{\varepsilon}_4))$ [32], where $\hat{\varepsilon}_4$ is the solution accuracy of IPM. In addition, **Steps** 10∼14 result in $\mathcal{O}(V_m K)$ comparisons. Hence, the total computational complexity of **Algorithm 4** is $\mathcal{O}(VK + \sum_{m=1}^{M} I_{4m}(KV_m)^{3.5} \log_2(1/\hat{\varepsilon}_4))$, where I_{4m} is the iteration number of the loop for the problem (P3-2).

In **Algorithm 5**, the iteration number of SFP is $\mathcal{O}((ML + V)^{0.5} \log_2(1/\varepsilon_6))$ [26]. Besides, the IPM in **Step** 8 leads to the complexity of $\mathcal{O}((ML + V)^{3.5} \log_2(1/\hat{\varepsilon}_5))$, where $\hat{\varepsilon}_5$ is the solution accuracy of IPM. Therefore, the total computational complexity of **Algorithm 5** is $\mathcal{O}(I_5(ML + V)^4 \log_2(1/\varepsilon_6) \log_2(1/\hat{\varepsilon}_5))$, where I_5 is the iteration number of the Dinkelbach method.

To sum up, the total computational complexity of the proposed resource allocation method is $\mathcal{O}(I_1(I_2(NZV + ZV^2 + V^3) + \sum_{m=1}^{M} \sum_{\tau=1}^{I_{3m}} (V_m L + \sum_{\hat{v}=1}^{|\mathcal{V}_m^{(\tau)}|} |\hat{\mathcal{L}}_{m,\hat{v}}^{(\tau)}| \log(|\hat{\mathcal{L}}_{m,\hat{v}}^{(\tau)}|)) + VK + \sum_{m=1}^{M} I_{4m}(KV_m)^{3.5} \log_2(1/\hat{\varepsilon}_4) + I_5(ML + V)^4 \log_2(1/\varepsilon_5) \log_2(1/\hat{\varepsilon}_5)))$.

V. Simulation Results

In this paper, the proposed BCD-based resource allocation algorithm for EE maximization in the IRS-assisted aggregated VLC-RF system is comprehensively evaluated by simulations. The simulation parameters are listed in Table I, which remain unchanged in this section unless otherwise stated. Moreover, five VLC APs are arranged along the road, with identical y-coordinates and z-coordinates of 0.97 m and 8.26 m, respectively, while the x-coordinates of VLC APs are 10 m, 30 m, 50 m, 70 m, and 90 m, respectively. Meanwhile, each OIRS is placed on a street lamp pole with the same x-coordinate as the corresponding VLC AP, while the y-coordinate is 0, and the bottommost unit is positioned at a z-coordinate of 3.75 m. In addition, the locations of RF AP and RF IRS are (50 m, 157 m, 10 m) and (50 m, −5 m, 10 m), respectively. Besides, the vehicles with the size of 4 m×2.2 m are randomly distributed on a two-lane road, with each lane having a width of 3.5 m. Furthermore, the height of the PD on each vehicle is 1 m. The IRS-assisted system in this section refers to the system assisted by both OIRS and RF IRS, whereas the OIRS-assisted and RF IRS-assisted system refers to the system aided by only OIRS and only RF IRS, respectively.

TABLE I
Simulation Parameters

	Parameter	Value
VLC	Number of VLC APs, M	5
	Lambertian index, κ	1
	Optical filter gain, Υ	1
	Semi-angle of PD's FOV, ψ_0	70°
	Refractive index of a PD, χ	1.5
	Area of PD, σ_v	1 cm^2
	Reflectivity of OIRS units, F	0.9
	Size of OIRS units	5 cm
	PSD of noise in VLC, μ_1	10^{-21} A^2/Hz
	Number of optical subchannels, L	40
	Bandwidth of each optical subchannel, W_1	0.5 MHz
	Maximum power of each VLC AP, $p_{m,\max}$	4 W
	Static power consumption of a VLC AP, U_1	1 W
	Static power consumption of an OIRS unit, U_3	0.01 W
	Number of OIRS units, K	30
RF	PSD of noise in RF, μ_2	-174 dBm/Hz
	Bandwidth of RF links, W_2	5 MHz
	Central carrier frequency of RF, f_c	5.9 GHz
	Number of antennas in RF AP, Z	16
	Path loss exponents, $\alpha_{0,v}$, α_1, $\alpha_{2,v}$	4.1, 2.1, 2.2
	Rician factor, ζ_1, ζ_2	3 dB, 3 dB
	Path loss at the reference distance, ρ	-40 dB
	Maximum power of the RF AP, $q_{\max}$	4 W
	Static power consumption of the RF AP, U_2	2 W
	Static power consumption of an RF IRS unit, U_4	0.01 W
	Number of RF IRS units, N	40
System	Power threshold $U_{\max}$	25 W
	Data rate constraint $R_{\min}$	4 Mbps
	Number of vehicles, V	13

A. Simulation of Convergence

Under diverse data rate constraints, the convergence performance of the proposed BCD-based algorithm during iterations is depicted in Fig. 2. It is evident that the proposed algorithm converges to a stationary point within four iterations, while a result close to the stationary point is obtained within two iterations. Furthermore, EE of the IRS-assisted aggregated system keeps rising in successive iterations, which verifies the convergence analysis in Section IV-E. With the increasing data rate constraint $R_{\min}$, more communication resources such as subchannels and powers are allocated to vehicles with weak channel gain to reach $R_{\min}$. Therefore, the EE achieved by the IRS-assisted aggregated system gradually decreases as $R_{\min}$ increases.

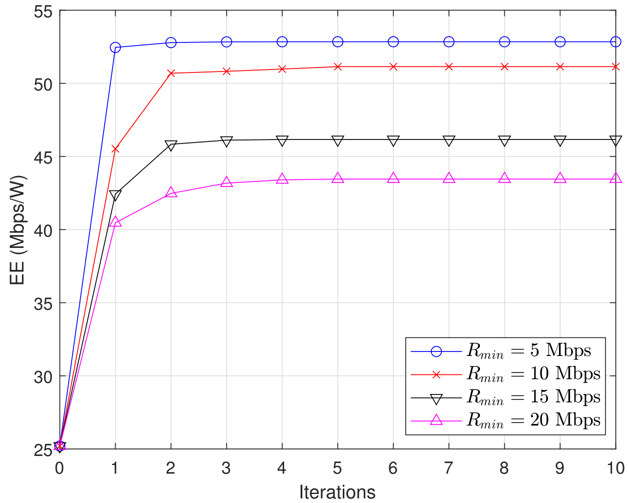

Fig. 2. Convergence of the proposed BCD-based resource allocation algorithm under different data rate constraints.

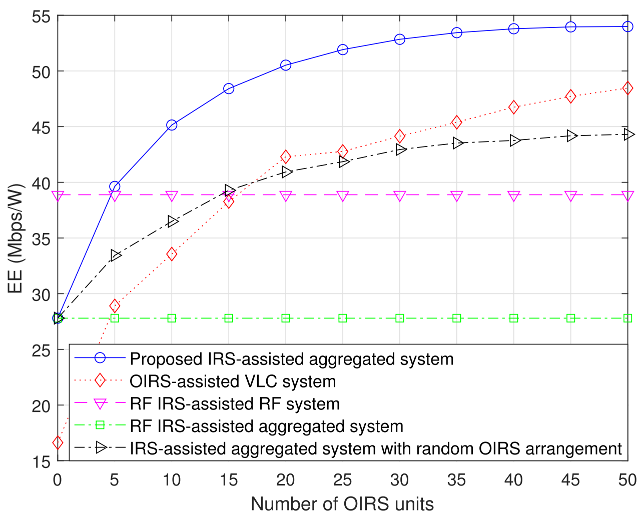

Fig. 3. The EE versus the unit number K of each OIRS for various systems.

B. Influence of the IRS Unit Number

To demonstrate the influence of the OIRS unit number on the IRS-assisted aggregated system, the EE of various systems versus the OIRS unit number is shown in Fig. 3. In addition, to illustrate the advantage of IRS-assisted aggregated VLC-RF system over IRS-assisted single systems in terms of EE improvement, the OIRS-assisted VLC system and RF IRS-assisted RF system are simulated, both of which are optimized according to the proposed BCD-based algorithm. Moreover, two methods are compared against MM-based OIRS arrangement, which are random arrangement and not using OIRS.

As the number of OIRS units K increases, the EE of the IRS-assisted aggregated system rises constantly, significantly surpassing that of the RF IRS-assisted aggregated system. This enhancement is attributed to OIRS units providing additional reflective VLC links, which strengthen the received signals while maintaining the same VLC power consumption, thereby resulting in a higher achievable data rate. Moreover, compared to IRS-assisted single systems, the IRS-assisted aggregated system also achieves higher EE, confirming its potential to improve EE. Conversely, when the number of OIRS units is small, the EE of the IRS-assisted aggregated system is lower than that of the RF IRS-assisted RF system. This is because the reflective links constructed by a few OIRS units only bring slight improvement of achievable data rate, whereas multiple VLC APs introduce high static power consumption. Furthermore, if OIRS units are allocated to vehicles randomly, the EE of the IRS-assisted aggregated system can also be improved due to the added OIRS reflection links, but the improvement is far less than that of the MM-based OIRS arrangement.

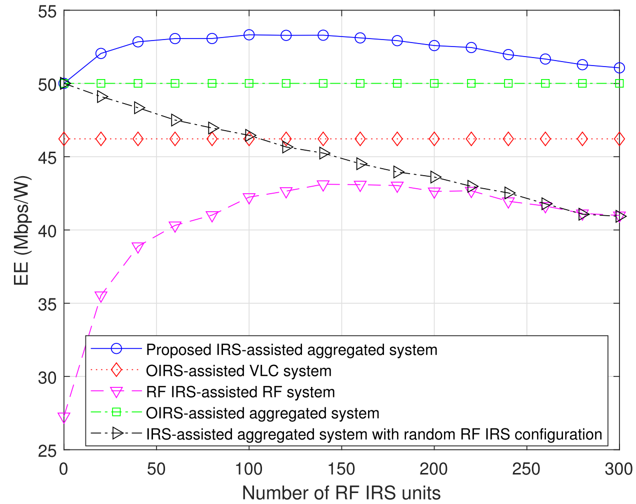

Fig. 4. The EE versus the unit number N of RF IRS for various systems.

The relationship between the number of RF IRS units N and the EE of the IRS-assisted aggregated system is presented in Fig. 4, in which the OIRS-assisted VLC system and RF IRS-assisted RF system are included as well. In addition, another two RF IRS configuration approaches are also simulated to verify the performance of GD-based RF IRS configuration, which are random configurations and not using RF IRS.

With the increase of N, the reconfiguration of the incident signal by RF IRS improves the RF channel gains, leading to the increasing EE of the IRS-assisted aggregated system. However, if N continues to increase, the achievable data rate enhancement brought by multiple RF IRS units is limited, while the static power consumption of RF IRS grows linearly, so the EE of the IRS-assisted aggregated system experiences a gradual decline. In contrast to the OIRS-assisted aggregated system, the addition of RF IRS improves the overall achievable data rate of all vehicles, subsequently improving EE. In addition, compared with EEs of IRS-assisted single systems, the EE of the IRS-assisted aggregated system is much higher, confirming the capability of IRS-assisted aggregated systems to improve EE. Additionally, if phases of RF IRS units are selected randomly, the signals reflected by RF IRS and those from RF AP to vehicles cannot be coherently combined, and thus the power consumption of the RF subsystem in the problem (P1) is not decreased. Besides, the static power consumption of RF IRS increases the total power consumption,

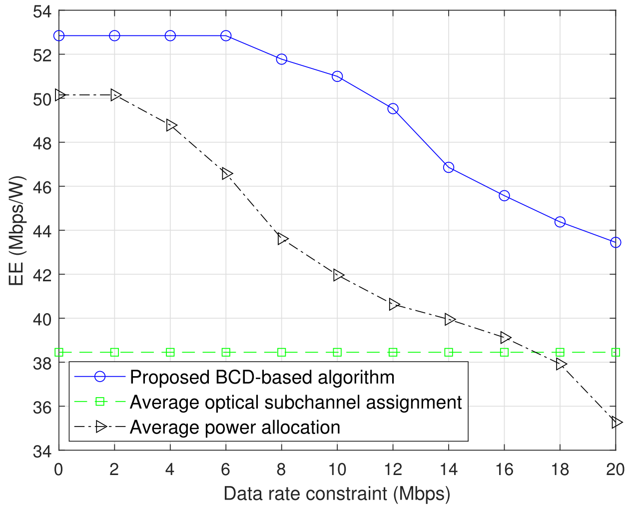

Fig. 5. The maximized EE under different data rate constraints.

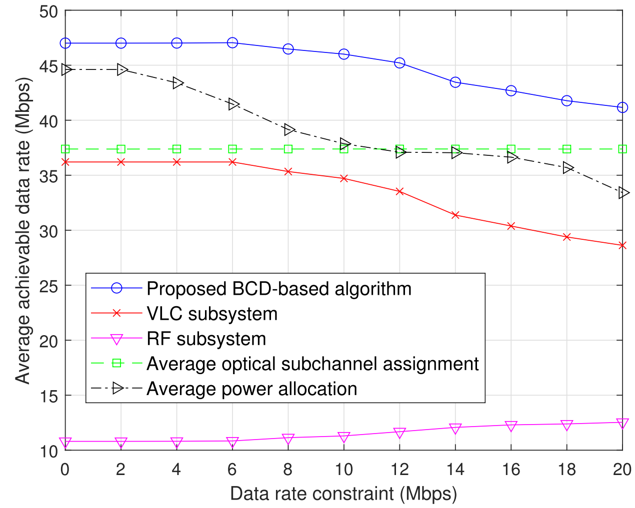

(a) The average achievable data rate among all vehicles.

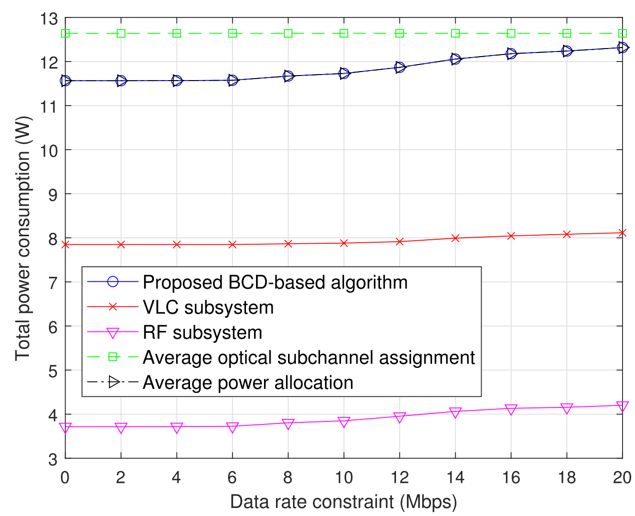

(b) Total power consumption.

Fig. 6. The average achievable data rate and the total power consumption with the maximized EE under different data rate constraints in diverse scenarios.

thereby decreasing EE of the IRS-assisted aggregated system to a level even lower than that of a system without RF IRS.

C. Influence of Data Rate Constraints

The influence of various data rate constraints on the proposed BCD-based resource allocation algorithm is investigated in Fig. 5, and the advantages of the proposed LRH-based optical subchannel assignment and Dinkelbach-based SFP joint power allocation are also illustrated. Meanwhile, the average achievable data rate among all vehicles and the total power consumption when EE of the IRS-assisted aggregated system reaches its maximum are shown in Fig. 6(a) and Fig. 6(b), respectively. Besides, the simulations in this section are conducted oriented to the IRS-assisted aggregated system.

As shown in Fig. 5, with the increase of $R_{\min}$, the EE achieved by the proposed BCD-based resource allocation algorithm initially remains constant and then decreases gradually. When $R_{\min}$ is less than the achievable data rate of each vehicle, the data rate constraint becomes invalid, leading to constant values for EE of the IRS-assisted aggregated system. As $R_{\min}$ continues to increase, the data rate constraint of some vehicles cannot be satisfied. Consequently, more resources such as optical subchannels and OIRS are reallocated from other vehicles to these vehicles to ensure the feasibility of data rate constraint. In this case, the achievable data rate obtained by utilizing the same resources becomes lower, resulting in a decreasing EE. For the same reason, the power consumption increases in both the VLC and RF subsystems in Fig. 6(b), while the achievable data rate of the VLC subsystem decreases in Fig. 6(a).

To verify the effectiveness of the Dinkelbach-based SFP joint power allocation, it is compared with the average joint power allocation. The average joint power allocation indicates that the non-static power consumption is uniformly distributed among all APs when the total power consumption is the same as that of the proposed BCD-based resource allocation algorithm. Then, the VLC AP and RF AP allocate power uniformly to each optical subchannel and each vehicle, respectively. According to Fig. 5, the EE achieved by average power allocation is much lower than that of Dinkelbach-based SFP joint power allocation. This disparity arises because the average power allocation fails to account for the differences in channel gains among vehicles, thereby preventing the attainment of a higher total achievable data rate as can be seen in Fig. 6(a).

To illustrate the advantages of the proposed LRH-based optical subchannel assignment, it is compared to the average optical subchannel assignment, which strives to distribute all optical subchannels of a VLC AP to vehicles served by this AP as equally as possible. For the LRH-based assignment, optical subchannels are assigned to satisfy the data rate constraints of all vehicles. Consequently, any surplus subchannels are assigned to vehicles with better channel conditions to achieve a higher achievable data rate under the same power consumption, while the achievable data rate of vehicles with poor channel gains is merely maintained at $R_{\min}$. In addition, as $R_{\min}$ grows, the optical subchannels also need to be reassigned to enhance the achievable data rate of these vehicles, leading to a decrease in the total achievable data rate,

TABLE II
MOBILITY INFORMATION ABOUT VEHICLES

Vehicle	Initial location	Speed	Path
1	Edge of a VLC cell	10 m/s	From the edge of the current VLC cell to its center
2	Edge of a VLC cell	20 m/s	From the edge of the current VLC cell to the edge of next VLC cell
3	Center of a VLC cell	10 m/s	From the center of the current VLC cell to its edge
4	Center of a VLC cell	20 m/s	From the center of the current VLC cell to the center of next VLC cell

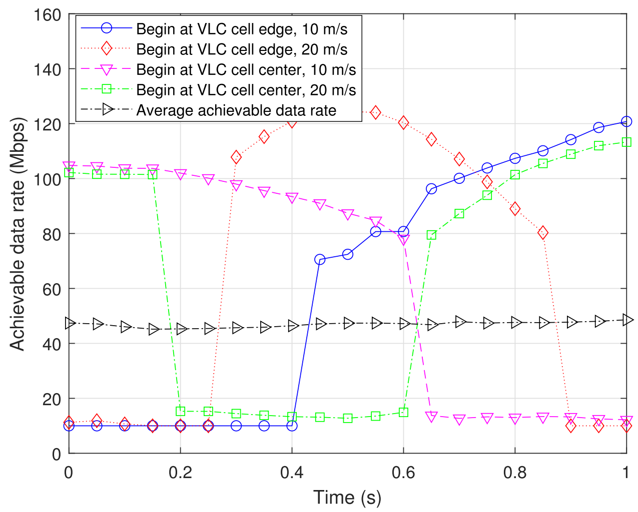

Fig. 7. The variation of achievable data rate with respect to time.

as shown in Fig. 6(a). In contrast, the average assignment allocates more subchannels to vehicles with weak channel gains, so the minimum achievable data rate among all vehicles is high when EE of the whole system reaches the maximum. Therefore, as illustrated in Fig. 5, the EE of the IRS-assisted aggregated system with average optical subchannel assignment remains relatively stable as $R_{\min}$ increases. In this case, while satisfying the data rate constraint, the remaining subchannels cannot be adopted to maximize the achievable data rate, thereby causing lower EE than that obtained by the LRH-based allocation, as revealed in Fig. 5.

D. Influence of Vehicle Mobility

With the intention of evaluating the influence of vehicle mobility on the IRS-assisted aggregated VLC-RF system, a simulation is carried out with a vehicle number of 13 and a data rate constraint set at 10 Mbps. For the purpose of focusing on the achievable data rate variation of vehicles in typical scenarios, the movements of four vehicles in different VLC cells are carefully designed, whose information is shown in Table II. Besides, for the other vehicles, their initial locations are random and their speeds are 10 m/s.

When a vehicle is positioned at the edge of a VLC cell, its achievable data rate remains close to the required data rate constraint, but it obtains a much higher achievable data rate when it is located at the center of a VLC cell. This result can be explained by the fact that while satisfying the data rate constraint for all vehicles, resources such as OIRS and power are allocated to vehicles located at the center of the VLC cell as much as possible due to their strong channel gain and free from interference. Consequently, these vehicles obtain high achievable data rates, enhancing the EE of the whole IRS-assisted aggregated system. In addition, as a vehicle approaches the center of a VLC cell, its channel gain increases gradually. When the channel gain of the vehicle becomes the largest within the VLC cell, more communication resources are allocated to the vehicle for the purpose of improving the EE, thereby bringing a fast increase in its achievable data rate. Conversely, a quick decrease in the achievable data rate also occurs when the vehicle moves away from the center of a VLC cell.

VI. CONCLUSION

In this paper, OIRS and RF IRS are utilized to assist the aggregated VLC-RF system, and the system model is established in detail. Besides, the resource allocation problem for EE maximization is formulated with the consideration of various constraints. Furthermore, the EE maximization problem is decomposed into four subproblems, and then iteratively solved by the proposed BCD-based resource allocation algorithm, finally obtaining a convergent solution. Specifically, the subproblems of RF IRS configuration, optical subchannel assignment, OIRS arrangement, and joint power allocation are optimized by GD, LRH algorithm, MM method, and Dinkelbach-based SFP, respectively. Moreover, numerical results indicate that the proposed BCD-based resource allocation algorithm converges quickly and outperforms other baselines with the aim of improving EE. Additionally, as the number of IRS units increases, the EE of the IRS-assisted aggregated system grows and significantly outperforms that of aggregated systems without IRS. In summary, OIRS and RF IRS can significantly enhance the EE of aggregated VLC-RF systems, showing great potential for future wireless communications.

APPENDIX A
PROOF OF LEMMA 1

To derive the partial derivative of $\Gamma_1(\boldsymbol{\theta})$ with respect to θ_n, the differential of $\Gamma_1(\boldsymbol{\theta})$ is derived as

$$\begin{aligned}
&\mathrm{d}\ \mathrm{tr}\left(\boldsymbol{E}\boldsymbol{Q}\boldsymbol{E}^H\right)\\
&=\mathrm{d}\ \mathrm{tr}\left(\boldsymbol{Q}\boldsymbol{E}^H\boldsymbol{E}\right) && \text{(50a)}\\
&=\mathrm{d}\ \mathrm{tr}\left(\boldsymbol{Q}\left(\boldsymbol{G}\boldsymbol{G}^H\right)^{-1}\right) && \text{(50b)}\\
&=-\mathrm{tr}\left(\hat{\boldsymbol{G}}\mathrm{d}\left(\boldsymbol{G}\boldsymbol{G}^H\right)\right) && \text{(50c)}\\
&=-\mathrm{tr}\left(\hat{\boldsymbol{G}}\mathrm{d}\left(\boldsymbol{G}^{(2)}\boldsymbol{\Phi}\boldsymbol{G}^{(1)}+\boldsymbol{G}^{(0)}\right)\boldsymbol{G}^H\right)\\
&\quad-\mathrm{tr}\left(\hat{\boldsymbol{G}}\boldsymbol{G}\mathrm{d}\left(\boldsymbol{G}^{(2)}\boldsymbol{\Phi}\boldsymbol{G}^{(1)}+\boldsymbol{G}^{(0)}\right)^H\right) && \text{(50d)}\\
&=-\sum_{n=1}^{N}\mathrm{tr}\left(\boldsymbol{G}^H\hat{\boldsymbol{G}}\tilde{\boldsymbol{G}}_n\mathrm{d}\phi_n\right)-\sum_{n=1}^{N}\mathrm{tr}\left(\tilde{\boldsymbol{G}}_n^H\hat{\boldsymbol{G}}\boldsymbol{G}\mathrm{d}\phi_n^*\right) && \text{(50e)}\\
&=-\sum_{n=1}^{N}2\mathrm{Re}\left\{je^{j\theta_n}\mathrm{tr}\left(\boldsymbol{G}^H\hat{\boldsymbol{G}}\tilde{\boldsymbol{G}}_n\right)\right\}\mathrm{d}\theta_n. && \text{(50f)}
\end{aligned}$$

$$\frac{\partial^2 \underline{R}_v}{\partial c_{m_1,l_1}\partial c_{m_2,l_2}} = \begin{cases} \varsigma_{vl_1}(t^2_{v,l_1,m_1} - \varrho_{v,l_1}t_{v,l_1,m_1}), & m_1 = m_2 \text{ and } l_1 = l_2, \\ \varsigma_{vl_1}t_{v,l_1,m_1}t_{v,l_1,m_2}, & m_1 \neq m_2 \text{ and } l_1 = l_2, \\ 0, & \text{otherwise.} \end{cases} \quad (56)$$

Eq. (50a) holds because of the properties of the trace. Due to the rule of matrix differential, Eq. (50c) and (50d) are guaranteed. Besides, on account of the definition of $\tilde{\boldsymbol{G}}_n$ and (8), Eq. (50e) is ensured. Based on the above derivation, the partial derivative (18) is proved.

Appendix B
Proof of Lemma 4

The second derivative of $\underline{R}_v(\hat{\boldsymbol{f}}_m)$ is represented as

$$\begin{aligned} &\frac{\partial^2 \underline{R}_v(\hat{\boldsymbol{f}}_m)}{\partial f_{m,k_1,v'}\partial f_{m,k_2,v}} \\ &= \frac{\partial}{\partial f_{m,k_1,v'}}\left[\frac{W_1}{\ln 2}\sum_{l=1}^{L} b_{m,v,l}r_{m,v,l}\frac{h^{(1)}_{v,k_2,m}}{h_{v,m}}\right] \\ &= \begin{cases} -\frac{W_1}{\ln 2}\sum_{l=1}^{L}\frac{b_{m,v,l}r_{m,v,l}}{h^2_{v,m}}h^{(1)}_{v,k_1,m}h^{(1)}_{v,k_2,m}, & v = v', \\ 0, & v \neq v'. \end{cases} \end{aligned} \quad (51)$$

Based on the definition of $\boldsymbol{h}^{(1)}_{v,m} = [h^{(1)}_{v,1,m}, \ldots, h^{(1)}_{v,K,m}]^T$, the Hessian matrix of $\underline{R}_v(\hat{\boldsymbol{f}}_m)$ with respect to $\hat{\boldsymbol{f}}_{m,v}$ is given by

$$\begin{aligned} \boldsymbol{D}_{m,v} &= \frac{\partial^2 \underline{R}_v(\hat{\boldsymbol{f}}_m)}{\partial \hat{\boldsymbol{f}}_{m,v}\partial \hat{\boldsymbol{f}}^T_{m,v}} \\ &= -\frac{W_1}{\ln 2}\sum_{l=1}^{L}\frac{b_{m,v,l}r_{m,v,l}}{h^2_{v,m}}\boldsymbol{h}^{(1)}_{v,m}(\boldsymbol{h}^{(1)}_{v,m})^T. \end{aligned} \quad (52)$$

For $\forall \boldsymbol{x} \in \mathbb{R}^{K\times 1}$ and $\boldsymbol{x} \neq \boldsymbol{0}$, the quadratic form of $\boldsymbol{D}_{m,v}$ is demonstrated as

$$\boldsymbol{x}^T\boldsymbol{D}_{m,v}\boldsymbol{x} = -\frac{W_1}{\ln 2}\sum_{l=1}^{L}\frac{b_{m,v,l}r_{m,v,l}}{h^2_{v,m}}\left(\boldsymbol{x}^T\boldsymbol{h}^{(1)}_{v,m}\right)^2 \leq 0, \quad (53)$$

which shows that $\boldsymbol{D}_{m,v}$ is a negative semidefinite matrix. The Hessian matrix of $\underline{R}_v(\hat{\boldsymbol{f}}_m)$ with respect to $\hat{\boldsymbol{f}}_m$ is given by

$$\overline{\boldsymbol{D}}_{m,v} = \frac{\partial^2 \underline{R}_v(\hat{\boldsymbol{f}}_m)}{\partial \hat{\boldsymbol{f}}_m\partial \hat{\boldsymbol{f}}^T_m} = \operatorname{diag}\left(\boldsymbol{O}, \ldots, \boldsymbol{O}, \boldsymbol{D}_{m,v}, \boldsymbol{O}, \ldots, \boldsymbol{O}\right). \quad (54)$$

It is obvious that $\overline{\boldsymbol{D}}_{m,v}$ is also a negative semidefinite matrix, and thus $\underline{R}_v(\hat{\boldsymbol{f}}_m)$ is a concave function of $\hat{\boldsymbol{f}}_m$.

Appendix C
Proof of Lemma 5

To simplify expressions, an auxiliary variable is defined as

$$t_{v,l,m} = (h^{(0)}_{v,m})^2(1 - a_{v,m})2^{c_{m,l}}, \quad (55)$$

and $\boldsymbol{t}_{v,l} = [t_{v,l,1}, \ldots, t_{v,l,M}]^T$. The second derivative of $\underline{R}_v(\boldsymbol{c})$ is represented as (56), shown at the top of the page, where $\varsigma_{v,l} = \ln 2/2\varrho^2_{v,l} \times W_1 b_{m_v,v,l}r_{m_v,v,l}$.

Therefore, the Hessian matrix of $\underline{R}_v(\boldsymbol{c})$ with respect to $\boldsymbol{c}_l$ is given by

$$\hat{\boldsymbol{D}}_{v,l} = \frac{\partial^2 \underline{R}_v(\boldsymbol{c})}{\partial \boldsymbol{c}_l\partial \boldsymbol{c}^T_l} = \varsigma_{v,l}\left[\boldsymbol{t}_{v,l}\boldsymbol{t}^T_{v,l} - \varrho_{v,l}\operatorname{diag}(\boldsymbol{t}_{v,l})\right]. \quad (57)$$

For $\forall \boldsymbol{x} \in \mathbb{R}^{M\times 1}$ and $\boldsymbol{x} \neq \boldsymbol{0}$, the quadratic form of $\hat{\boldsymbol{D}}_v$ is demonstrated as

$$\begin{aligned} &\boldsymbol{x}^T\hat{\boldsymbol{D}}_{v,l}\boldsymbol{x} \\ &= \varsigma_{v,l}\left[\boldsymbol{x}^T\boldsymbol{t}_{v,l}\boldsymbol{t}^T_{v,l}\boldsymbol{x} - \boldsymbol{x}^T\varrho_{v,l}\operatorname{diag}(\boldsymbol{t}_{v,l})\boldsymbol{x}\right] \\ &= \varsigma_{v,l}\left[\left(\boldsymbol{x}^T\boldsymbol{t}_{v,l}\right)^2 - \boldsymbol{x}^T\left(\boldsymbol{1}^T\boldsymbol{t}_{v,l} + \mu_1 W_1\right)\operatorname{diag}(\boldsymbol{t}_{v,l})\boldsymbol{x}\right] \\ &= \varsigma_{v,l}\left[\left(\hat{\boldsymbol{x}}^T\hat{\boldsymbol{t}}_{v,l}\right)^2 - \left(\hat{\boldsymbol{t}}^T_{v,l}\hat{\boldsymbol{t}}_{v,l}\right)\left(\hat{\boldsymbol{x}}^T\hat{\boldsymbol{x}}\right) - \mu_1 W_1\hat{\boldsymbol{x}}^T\hat{\boldsymbol{x}}\right] \\ &\leq -\mu_1 W_1\hat{\boldsymbol{x}}^T\hat{\boldsymbol{x}} \leq 0, \end{aligned} \quad (58)$$

where the inequality holds due to Cauchy-Schwarz inequality and $\hat{\boldsymbol{x}} = [x_1\sqrt{t_{v,l,1}}, \ldots, x_M\sqrt{t_{v,l,M}}]^T$, $\hat{\boldsymbol{t}}_{v,l} = [\sqrt{t_{v,l,1}}, \ldots, \sqrt{t_{v,l,M}}]^T$. The negativity of quadratic form implies that $\hat{\boldsymbol{D}}_{v,l}$ is a negative semidefinite matrix. Moreover, the Hessian matrix of $\underline{R}_v(\boldsymbol{c})$ with respect to $\boldsymbol{c}$ is given by

$$\hat{\boldsymbol{D}}_v = \frac{\partial^2 \underline{R}_v(\boldsymbol{c})}{\partial \boldsymbol{c}\partial \boldsymbol{c}^T} = \operatorname{diag}\left(\hat{\boldsymbol{D}}_{v,1}, \ldots, \hat{\boldsymbol{D}}_{v,L}\right). \quad (59)$$

It is easy to show that $\hat{\boldsymbol{D}}_v$ is also a negative semidefinite matrix, thus $\underline{R}_v(\boldsymbol{c})$ is a concave function of $\boldsymbol{c}$.

According to (13), $S_v(\boldsymbol{q})$ is a function of q_v in logarithmic form, thus it is a concave function of $\boldsymbol{q}$. Due to the summation form of $\underline{R}_T$, the concavity of $\underline{R}_T$ holds, proving Lemma 5.

References

[1] N. An, F. Yang, L. Cheng, J. Song, and Z. Han, "Resource allocation for aggregated VLC-RF system with OIRS on energy efficiency," accepted by IEEE Int. Conf. Commun. (ICC), Jun. 2024, pp. 1–6.

[2] W. Saad, M. Bennis, and M. Chen, "A vision of 6G wireless systems: Applications, trends, technologies, and open research problems," *IEEE Netw.*, vol. 34, no. 3, pp. 134–142, May 2020.

[3] M. Kashef, M. Ismail, M. Abdallah, K. A. Qaraqe, and E. Serpedin, "Energy efficient resource allocation for mixed RF/VLC heterogeneous wireless networks," *IEEE J. Sel. Areas Commun.*, vol. 34, no. 4, pp. 883–893, Apr. 2016.

[4] M. Obeed, A. M. Salhab, M.-S. Alouini, and S. A. Zummo, "On optimizing VLC networks for downlink multi-user transmission: A survey," *IEEE Commun. Surveys Tuts.*, vol. 21, no. 3, pp. 2947–2976, 3rd Quart., 2019.

[5] F. Wang, F. Yang, J. Song, and Z. Han, "Access frameworks and application scenarios for hybrid VLC and RF systems: State of the art, challenges, and trends," *IEEE Commun. Mag.*, vol. 60, no. 3, pp. 55–61, Mar. 2022.

[6] X. Wu, M. Safari, and H. Haas, "Access point selection for hybrid Li-Fi and Wi-Fi networks," *IEEE Trans. Commun.*, vol. 65, no. 12, pp. 5375–5385, Dec. 2017.

[7] S. Ma, F. Zhang, H. Li, F. Zhou, M. Alouini, and S. Li, "Aggregated VLC-RF systems: Achievable rates, optimal power allocation, and energy efficiency," *IEEE Trans. Wireless Commun.*, vol. 19, no. 11, pp. 7265–7278, Nov. 2020.

[8] S. Aboagye, T. M. N. Ngatched, O. A. Dobre, and H. V. Poor, "Energy-efficient resource allocation for aggregated RF/VLC systems," *IEEE Trans. Wireless Commun.*, vol. 22, no. 10, pp. 6624–6640, Oct. 2023.

[9] S. Shao et al., "Design and analysis of a visible-light-communication enhanced WiFi system," *IEEE J. Opt. Commun. Netw.*, vol. 7, no. 10, pp. 960–973, Oct. 2015.

[10] S. Aboagye, T. M. N. Ngatched, O. A. Dobre, and A. Ibrahim, "Joint access point assignment and power allocation in multi-tier hybrid RF/VLC HetNets," *IEEE Trans. Wireless Commun.*, vol. 20, no. 10, pp. 6329–6342, Oct. 2021.

[11] S. Ma et al., "Optimal discrete constellation inputs for aggregated LiFi-WiFi networks," *IEEE Trans. Wireless Commun.*, vol. 21, no. 6, pp. 3979–3993, Jun. 2022.

[12] H. Zhang, N. Liu, K. Long, J. Cheng, V. C. M. Leung, and L. Hanzo, "Energy efficient subchannel and power allocation for software-defined heterogeneous VLC and RF networks," *IEEE J. Sel. Areas Commun.*, vol. 36, no. 3, pp. 658–670, Mar. 2018.

[13] F. Wang, F. Yang, C. Pan, J. Song, and Z. Han, "Hybrid VLC-RF systems with multi-users for achievable rate and energy efficiency maximization," *IEEE Trans. Wireless Commun.*, vol. 22, no. 9, pp. 6157–6170, Sep. 2023.

[14] J. Chen, Z. Wang, and T. Mao, "Resource management for hybrid RF/VLC V2I wireless communication system," *IEEE Commun. Lett.*, vol. 24, no. 4, pp. 868–871, Apr. 2020.

[15] X. Shi, J. Wang, and J. Song, "Triple-structured compressive sensing-based channel estimation for RIS-aided MU-MIMO systems," *IEEE Trans. Wireless Commun.*, vol. 21, no. 12, pp. 11095–11109, Dec. 2022.

[16] N. V. Deshpande, S. Dey, D. N. Amudala, and R. Budhiraja, "Spatially-correlated IRS-aided multiuser FD mMIMO systems: Analysis and optimization," *IEEE Trans. Commun.*, vol. 70, no. 6, pp. 3879–3896, Jun. 2022.

[17] H. Guo, Y.-C. Liang, J. Chen, and E. G. Larsson, "Weighted sum-rate maximization for reconfigurable intelligent surface aided wireless networks," *IEEE Trans. Wireless Commun.*, vol. 19, no. 5, pp. 3064–3076, May 2020.

[18] H. Zhang, S. Ma, Z. Shi, X. Zhao, and G. Yang, "Sum-rate maximization of RIS-aided multi-user MIMO systems with statistical CSI," *IEEE Trans. Wireless Commun.*, vol. 22, no. 7, pp. 4788–4801, Jul. 2023.

[19] H. Xie, J. Xu, and Y.-F. Liu, "Max-min fairness in IRS-aided multi-cell MISO systems with joint transmit and reflective beamforming," *IEEE Trans. Wireless Commun.*, vol. 20, no. 2, pp. 1379–1393, Feb. 2021.

[20] S. Atapattu, R. Fan, P. Dharmawansa, G. Wang, J. Evans, and T. A. Tsiftsis, "Reconfigurable intelligent surface assisted two-way communications: Performance analysis and optimization," *IEEE Trans. Commun.*, vol. 68, no. 10, pp. 6552–6567, Oct. 2020.

[21] Y. Wang, W. Shi, M. Huang, F. Shu, and J. Wang, "Intelligent reflecting surface aided secure transmission with colluding eavesdroppers," *IEEE Trans. Veh. Technol.*, vol. 71, no. 9, pp. 10155–10160, Sep. 2022.

[22] W. Shi, Q. Wu, F. Xiao, F. Shu, and J. Wang, "Secrecy throughput maximization for IRS-aided MIMO wireless powered communication networks," *IEEE Trans. Commun.*, vol. 70, no. 11, pp. 7520–7535, Nov. 2022.

[23] Q. Wu and R. Zhang, "Joint active and passive beamforming optimization for intelligent reflecting surface assisted SWIPT under QoS constraints," *IEEE J. Sel. Areas Commun.*, vol. 38, no. 8, pp. 1735–1748, Aug. 2020.

[24] N. Li et al., "Min–max latency optimization for IRS-aided cell-free mobile edge computing systems," *IEEE Internet Things J.*, vol. 11, no. 5, pp. 8757–8770, Mar. 2024.

[25] C. Huang, A. Zappone, G. C. Alexandropoulos, M. Debbah, and C. Yuen, "Reconfigurable intelligent surfaces for energy efficiency in wireless communication," *IEEE Trans. Wireless Commun.*, vol. 18, no. 8, pp. 4157–4170, Aug. 2019.

[26] Z. Yang et al., "Energy-efficient wireless communications with distributed reconfigurable intelligent surfaces," *IEEE Trans. Wireless Commun.*, vol. 21, no. 1, pp. 665–679, Jan. 2022.

[27] Z. Li et al., "Energy efficient reconfigurable intelligent surface enabled mobile edge computing networks with NOMA," *IEEE Trans. Cogn. Commun. Netw.*, vol. 7, no. 2, pp. 427–440, Jun. 2021.

[28] L. You, J. Xiong, D. W. K. Ng, C. Yuen, W. Wang, and X. Gao, "Energy efficiency and spectral efficiency tradeoff in RIS-aided multiuser MIMO uplink transmission," *IEEE Trans. Signal Process.*, vol. 69, pp. 1407–1421, 2021.

[29] S. Aboagye, A. R. Ndjiongue, T. M. N. Ngatched, O. A. Dobre, and H. V. Poor, "RIS-assisted visible light communication systems: A tutorial," *IEEE Commun. Surveys Tuts.*, vol. 25, no. 1, pp. 251–288, 1st Quart., 2023.

[30] S. Sun, F. Yang, J. Song, and Z. Han, "Joint resource management for intelligent reflecting surface-aided visible light communications," *IEEE Trans. Wireless Commun.*, vol. 21, no. 8, pp. 6508–6522, Aug. 2022.

[31] S. Sun, W. Mei, F. Yang, N. An, J. Song, and R. Zhang, "Optical intelligent reflecting surface assisted MIMO VLC: Channel modeling and capacity characterization," *IEEE Trans. Wireless Commun.*, vol. 23, no. 3, pp. 2125–2139, Mar. 2024.

[32] B. Cao, M. Chen, Z. Yang, M. Zhang, J. Zhao, and M. Chen, "Reflecting the light: Energy efficient visible light communication with reconfigurable intelligent surface," in *Proc. IEEE 92nd Veh. Technol. Conf. (VTC-Fall)*, Victoria, BC, Canada, Nov. 2020, pp. 1–5.

[33] C. Xu et al., "Channel estimation for reconfigurable intelligent surface assisted high-mobility wireless systems," *IEEE Trans. Veh. Technol.*, vol. 72, no. 1, pp. 718–734, Jan. 2023.

[34] Z. Huang, B. Zheng, and R. Zhang, "Roadside IRS-aided vehicular communication: Efficient channel estimation and low-complexity beamforming design," *IEEE Trans. Wireless Commun.*, vol. 22, no. 9, pp. 5976–5989, Sep. 2023.

[35] Y. Chen, Y. Wang, and Z. Wang, "Reconfigurable intelligent surface aided high-mobility millimeter wave communications with dynamic dual-structured sparsity," *IEEE Trans. Wireless Commun.*, vol. 22, no. 7, pp. 4580–4599, Jul. 2023.

[36] A. M. Abdelhady et al., "Channel characterization of IRS-based visible light communication systems," *IEEE Trans. Commun.*, vol. 70, no. 3, pp. 1913–1926, Mar. 2022.

[37] A. M. Abdelhady, A. K. S. Salem, O. Amin, B. Shihada, and M.-S. Alouini, "Visible light communications via intelligent reflecting surfaces: Metasurfaces vs mirror arrays," *IEEE Open J. Commun. Soc.*, vol. 2, pp. 1–20, 2021.

[38] V. Jamali, H. Ajam, M. Najafi, B. Schmauss, R. Schober, and H. V. Poor, "Intelligent reflecting surface assisted free-space optical communications," *IEEE Commun. Mag.*, vol. 59, no. 10, pp. 57–63, Oct. 2021.

[39] Y. Chen, Y. Wang, J. Zhang, and Z. Li, "Resource allocation for intelligent reflecting surface aided vehicular communications," *IEEE Trans. Veh. Technol.*, vol. 69, no. 10, pp. 12321–12326, Oct. 2020.

[40] Y. Han, W. Tang, S. Jin, C.-K. Wen, and X. Ma, "Large intelligent surface-assisted wireless communication exploiting statistical CSI," *IEEE Trans. Veh. Technol.*, vol. 68, no. 8, pp. 8238–8242, Aug. 2019.

[41] A. Alizadeh and M. Vu, "Load balancing user association in millimeter wave MIMO networks," *IEEE Trans. Wireless Commun.*, vol. 18, no. 6, pp. 2932–2945, Jun. 2019.

[42] T. Öncan, "A survey of the generalized assignment problem and its applications," *Inf. Syst. Oper. Res.*, vol. 45, no. 3, pp. 123–141, Aug. 2007.

[43] M. Held and R. M. Karp, "The traveling-salesman problem and minimum spanning trees—Part II," *Math. Program.*, vol. 1, no. 1, pp. 6–25, Dec. 1971.

[44] M. Bohge, J. Gross, A. Wolisz, and M. Meyer, "Dynamic resource allocation in OFDM systems: An overview of cross-layer optimization principles and techniques," *IEEE Netw.*, vol. 21, no. 1, pp. 53–59, Jan. 2007.

[45] Y. Sun, P. Babu, and D. P. Palomar, "Majorization-minimization algorithms in signal processing, communications, and machine learning," *IEEE Trans. Signal Process.*, vol. 65, no. 3, pp. 794–816, Feb. 2017.

[46] J. Papandriopoulos and J. Evans, "Low-complexity distributed algorithms for spectrum balancing in multi-user DSL networks," in *Proc. IEEE Int. Conf. Commun.*, Jun. 2006, pp. 3270–3275.

[47] B. R. Marks and G. P. Wright, "A general inner approximation algorithm for nonconvex mathematical programs," *Oper. Res.*, vol. 26, no. 4, pp. 681–683, Aug. 1978.

[48] W. Dinkelbach, "On nonlinear fractional programming," *Manag. Sci.*, vol. 13, no. 7, pp. 492–498, Mar. 1967.

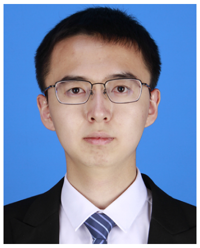

Nan An received the B.S. degree from the Department of Electronic Engineering, Tsinghua University, Beijing, China, in 2021, where he is currently pursuing the Ph.D. degree with the DTV Technology Research and Development Center, Department of Electronic Engineering. His research interests are in the field of visible light communications, wireless communications, and vehicular communication.

Fang Yang (Senior Member, IEEE) received the B.S.E. and Ph.D. degrees in electronic engineering from Tsinghua University, Beijing, China, in 2005 and 2009, respectively. He is currently an Associate Professor with the Department of Electronic Engineering, Tsinghua University. He has published over 180 peer-reviewed journal and conference papers. He holds over 50 Chinese patents and two PCT patents. His research interests are in the fields of power line communication, visible light communication, wireless communication, and digital television terrestrial broadcasting. He is a fellow of IET. He received the IEEE Scott Helt Memorial Award (Best Paper Award in the IEEE TRANSACTIONS ON BROADCASTING) in 2015. He is the Secretary General of Sub-Committee 25 of the China National Information Technology Standardization (SAC/TC28/SC25). He currently serves as an Associate Editor for the IEEE TRANSACTIONS ON GREEN COMMUNICATIONS AND NETWORKING and *IET Optoelectronics*.

Ling Cheng (Senior Member, IEEE) received the B.Eng. degree (cum laude) in electronics and information from Huazhong University of Science and Technology (HUST) in 1995, and the M.-Ing. degree (cum laude) in electrical and electronics and the D.-Ing. degree electrical and electronics from the University of Johannesburg (UJ), in 2005 and 2011, respectively. In 2010, he joined the University of the Witwatersrand, where he was promoted to a Full Professor in 2019. He has been a Visiting Professor with five universities and the principal advisor for over 40 full research post-graduate students. He has published more than 100 research papers in journals and conference proceedings. His research interests are in telecommunications and artificial intelligence. He received the Chancellor's Medals in 2005 and 2019, the National Research Foundation ratings in 2014 and 2020, and the IEEE ISPLC 2015 Best Student Paper Award was made to his Ph.D. student in Austin. He is the Vice-Chair of IEEE South African Information Theory Chapter. He serves as an associate editor for three journals.

Jian Song (Fellow, IEEE) received the B.Eng. and Ph.D. degrees in electrical engineering from Tsinghua University, Beijing, China, in 1990 and 1995, respectively. He is currently the Director of Tsinghua DTV Technology Research and Development Center, Tsinghua University. He has been working in quite different areas, including fiber-optic, satellite, and wireless communications; and the power-line communications. He holds two U.S. and more than 80 Chinese patents. He has published more than 300 peer-reviewed journal and conference papers and coauthored several books in the aforementioned areas. His current research interest is in the area of digital TV broadcasting, network convergence, and visible light communication networks. He is a fellow of IET, the Chinese Institute of Electronics, and the Chinese Institute of Communications. He won several awards both international and domestic.

Zhu Han (Fellow, IEEE) received the B.S. degree in electronic engineering from Tsinghua University in 1997, and the M.S. and Ph.D. degrees in electrical and computer engineering from the University of Maryland, College Park, in 1999 and 2003, respectively.

From 2000 to 2002, he was a Research and Development Engineer of JDSU, Germantown, MD, USA. From 2003 to 2006, he was a Research Associate with the University of Maryland. From 2006 to 2008, he was an Assistant Professor with Boise State University, Idaho. Currently, he is a John and Rebecca Moores Professor with the Electrical and Computer Engineering Department and the Computer Science Department, University of Houston, TX, USA. His main research targets on the novel game-theory related concepts critical to enabling efficient and distributive use of wireless networks with limited resources. His other research interests include wireless resource allocation and management, wireless communications and networking, quantum computing, data science, smart grids, carbon neutralization, security, and privacy. He received the NSF Career Award in 2010, the Fred W. Ellersick Prize of the IEEE Communication Society in 2011, the EURASIP Best Paper Award for the *Journal on Advances in Signal Processing* in 2015, the IEEE Leonard G. Abraham Prize in the field of Communications Systems (Best Paper Award in IEEE JSAC) in 2016, IEEE Vehicular Technology Society 2022 Best Land Transportation Paper Award, and several best paper awards in IEEE conferences. He was the Winner of the 2021 IEEE Kiyo Tomiyasu Award (an IEEE Field Award), for outstanding early to mid-career contributions to technologies holding the promise of innovative applications, with the following citation: "for contributions to game theory and distributed management of autonomous communication networks." He was an IEEE Communications Society Distinguished Lecturer, from 2015 to 2018; an ACM Distinguished Speaker, from 2022 to 2025; an AAAS Fellow, since 2019; and an ACM Fellow, since 2024. He is a 1% highly cited researcher since 2017 according to Web of Science.